**Hydrogen storage properties of lithium aluminohydride
modified by dopants and mechanochemistry**

by

Keita Hosokawa

A thesis submitted to the graduate faculty

in partial fulfillment of the requirements for the degree of

MASTER OF SCIENCE

Major: Materials Science and Engineering

Program of Study Committee:
Vitalij K. Pecharsky, Major Professor
Gordon J. Miller
Karl A. Gschneidner, Jr.

Iowa State University

Ames, Iowa

2002

Graduate College
Iowa State University

This is to certify that the master's thesis of

Keita Hosokawa

has met the thesis requirements of Iowa State University

_____

Major Professor

_____

For the Major Program

TABLE OF CONTENTS

ABSTRACT

Alkali metal aluminohydrides have high potential as solid hydrogen storage materials. They have been known for their irreversible dehydrogenation process below 100 atm until Bogdanovic et al [1, 2] succeeded in the re-hydrogenation of $NaAlH_4$ below 70 atm. They achieved 4 wt.% H_2 reversible capacity by doping $NaAlH_4$ with Ti and/or Fe organo-metalic compounds as catalysts. This suggests that other alkali and, possibly alkaline earth metal aluminohydrides can be used for reversible hydrogen storage when modified by proper dopants.

In this research, $Zr_{27}Ti_9Ni_{38}V_5Mn_{16}Cr_5$, $LaNi_{4.85}Sn_{0.15}$, Al_3Ti, and $PdCl_2$ were combined with $LiAlH_4$ by ball-milling to study whether or not $LiAlH_4$ is capable to both absorb and desorb hydrogen near ambient conditions. X-ray powder diffraction, differential thermal analysis, and scanning electron microscopy were employed for sample characterizations. All four compounds worked as catalysts in the dehydrogenation reactions of both $LiAlH_4$ and Li_3AlH_6 by inducing the decomposition at lower temperature. However, none of them was applicable as catalyst in the reverse hydrogenation reaction at low to moderate hydrogen pressure.

1. INTRODUCTION

1.1 General Background

Energy Shift

Many modern environmental problems are associated with our use of energy. In addition to the expected depletion of fossil fuel reserves, air pollution, acid rain, and global warming are all the results of over consumption of oil, coal, and natural gas. For many years researchers in both academia and industry have been seeking alternative energy sources, which are both renewable and environmentally benign. One of the alternative energy resources is pure hydrogen. When hydrogen reacts with oxygen, the energy of its oxidation can be converted into heat or electricity. Since the reaction of hydrogen with oxygen produces only water, hydrogen is the best alternative source of energy from the environmental standpoint. Moreover, hydrogen can be obtained from water during electrolysis, or via chemical or biochemical conversion of agricultural products, and therefore dependence on certain countries or regions for a steady supply of energy can be reduced.

How to derive energy from hydrogen ?

Chemical energy of hydrogen oxidation may be converted into thermal and then mechanical energy in a conventional internal combustion engine. Hydrogen has more benefits than gasoline as an automotive fuel: (i) the combustion of hydrogen in the air generates high temperature and yields NO_x, but their amount is only 20% of the amount generated in a gasoline powered engine [3]; (ii) the energy density per unit mass of hydrogen (28,700 kcal/kg) is almost three times higher than that of gasoline (10,630 kcal/kg); (iii) the amount of CO_2 generated by the combustion of hydrogen is zero, while the combustion of gasoline generates about 2.27 kg CO_2/Q, where Q=heat value of 1 litter of gasoline. Moreover, since the minimum energy required for ignition of hydrogen is almost an order of magnitude lower than that of gasoline, hydrogen

can be mixed with larger amount of air than gasoline, which enables a more complete combustion reaction and thus better efficiency. Unfortunately this also leads to a drawback, i.e., premature ignition or flashback may result because of hot gases or hot spots in a cylinder [4].

Another way to use the chemical energy of the hydrogen oxidation is to directly convert it into the electrical energy. In this case, a fuel cell may be used. Figure 1 illustrates the principle of a polymer electrolyte fuel cell (PEFC). When hydrogen enters the fuel cell, a platinum catalyst on anode separates it into hydrogen ions and electrons. The electrons pass through an electrical circuit and are combined with oxygen on the cathode with the help of platinum. The hydrogen ions pass through the electrolyte membrane, react with oxygen ions on the cathode, and then become water [5]. The major advantage of a fuel cell is its high energy conversion efficiency. When the heat produced by the fuel cell is used, its total energy conversion efficiency can reach 80%. On the other hand, since the conventional power plant first converts the chemical energy into the thermal energy, and then into the electrical energy, the overall efficiency is only about 40 % or less [6]. However, fuel cells require further improvements. Durability is one of the practical problems. Electrodes and electrolytes may be poisoned by carbon dioxide, carbon monoxide, or sulfur compounds, or even self-degrade due to the diffusion of their elements. In the case of a breakdown of an electrolyte membrane, a large amount of hydrogen and oxygen or air are mixed together and an explosion may result. Electrocatalysts and materials for electrodes and electrolyte membrane have been studied extensively for better performance. Eventually, expensive materials must be replaced by more affordable ones [7].
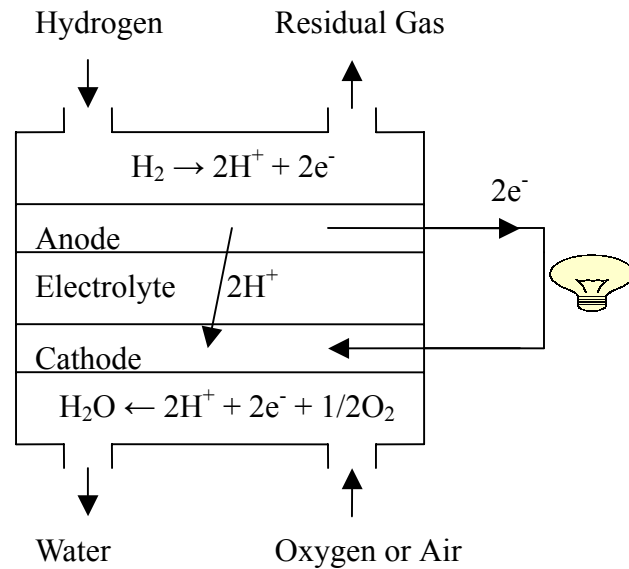
$$H_2 \rightarrow 2H^+ + 2e^-$$

Hydrogen   Residual Gas

$2e^-$

Anode

Electrolyte $2H^+$

Cathode

$$H_2O \leftarrow 2H^+ + 2e^- + 1/2O_2$$

Water   Oxygen or Air

Figure1. A schematic of a polymer electrolyte fuel cell.
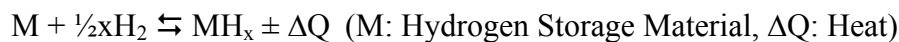

Hydrogen Storage

Although hydrogen itself is perceived by many people as an ideal fuel, its storage, delivery, and distribution remain problematic. There are three ways to store hydrogen: gaseous, liquid, and solid-state storage. In the solid state, hydrogen is absorbed by or bonded to the materials called hydrogen storage materials. Of the three hydrogen storage approaches mentioned above, the solid state storage has the highest volumetric density of hydrogen, which is about 8 times higher than that of the compressed gas (at 150 atm), and somewhat higher than that of liquid hydrogen. This means that hydrogen storage solids can store hydrogen in the most compact way. Moreover, while hydrogen storage materials can store hydrogen at ambient temperature and pressure, gaseous and liquid-state storages require extremely high pressure, or extremely low temperature, respectively. Therefore solid-state storage is the safest, most convenient, and hence, most suitable way of storing and distributing hydrogen. However, the solid-state storage also has drawbacks. If one compares the weight fraction of hydrogen in hydrogen storage materials with that of liquid carbohydrates, e.g. oil, the latter have much higher

mass density of hydrogen than that of most hydrogen storage solids. This parameter must be improved before solid state storage of hydrogen becomes practical.

Reforming gasoline, natural gas, methanol, or methane to produce hydrogen is a good way to avoid the immediate distribution infrastructure problem. However, reforming requires additional equipment and energy, and it is not pollution-free. Moreover, it does not address the issue of depletion of fossil fuels. Therefore in the long term a shift to hydrogen-based energy coupled with advanced hydrogen storage materials appears to be the best alterative to current fossil fuels-based energy sector [8].

Other Potential Uses of Hydrogen Storage Materials

Hydrogen absorption and desorption involves heat:

$M + \frac{1}{2}xH_2 \leftrightarrows MH_x \pm \Delta Q$ (M: Hydrogen Storage Material, ΔQ: Heat)

This property may be used for heat pumping, when two hydrogen storage materials which have different hydrogen equilibrium pressure are used. Figure 2 illustrates the principle of the cooling and the heating systems. $(MH_x)^l$ is the hydrogen storage material which has the hydrogen equilibrium pressure lower than that of another hydrogen storage material, $(MH_x)^h$. In the cooling system, $(MH_x)^l$ releases hydrogen when it is heated up. The increased hydrogen pressure creates $(MH_x)^h$ and the generated heat is released outside (a). When the heating of $(M)^l$ is stopped, $(MH_x)^h$ releases hydrogen and absorbs the heat, and $(M)^l$ absorbs hydrogen and releases the generated heat outside because of the difference of the hydrogen equilibrium pressures (b). In the heating system the principle is the same, but the heat is released inside. The efficiency increases when several sets of two different hydrogen storage materials are used [9].
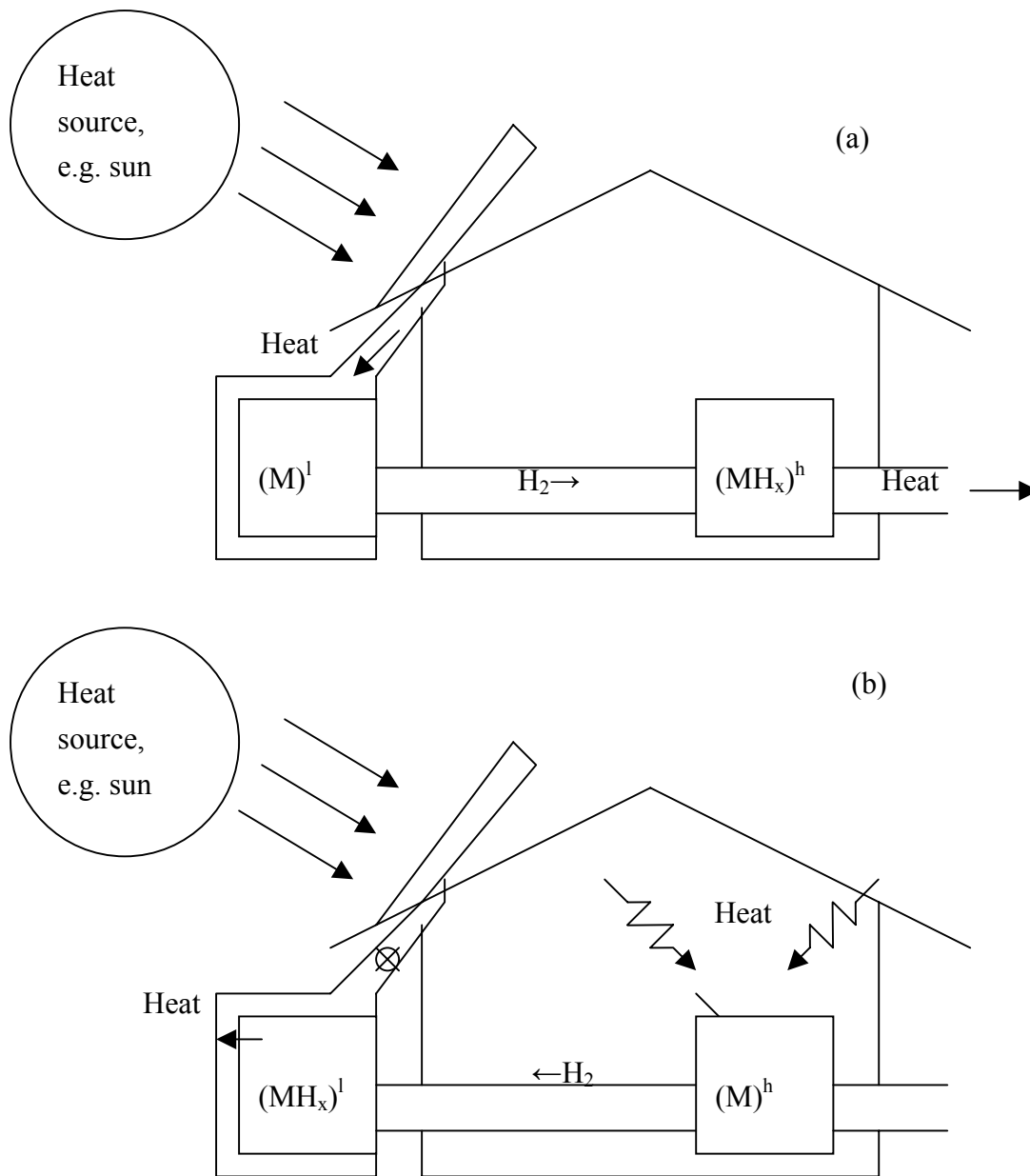
Figure 2. The principle of the cooling system using two solid state hydrides with different equilibrium hydrogen pressure. $(MH_x)^l$ - hydride with low equilibrium pressure, $(MH_x)^h$ - hydride with high equilibrium pressure.

Hydrogen storage materials are also used in secondary batteries, metal hydride-nickel hydroxide cells. Figure 3 is the schematic of this cell. The reactions at the electrodes are as follows:

Positive: $Ni(OH)_2 + OH^- \leftrightarrows NiOOH + H_2O + e^-$

Negative: $M + H_2O + e^- \leftrightarrows MH + OH^-$ $\leftarrow$: Discharging process

Total: $M + Ni(OH)_2 \leftrightarrows MH + NiOOH$ $\rightarrow$: Charging process

Metal hydride-nickel hydroxide cells have large advantages in both volumetric energy density and environmental benignity when compared with lead-acid and nickel-cadmium cells. The volumetric energy density of metal hydride-nickel hydroxide cells is about twice higher than that of nickel-cadmium cells, and $LaNi_5$- or $ZrNi_2$-based alloys pose lower environmental hazard than lead- or cadmium-based batteries. Although gravimetric and volumetric energy densities of metal hydride-nickel hydroxide cells are lower than those of rechargeable lithium cells, metal hydride-nickel hydroxide cells have advantages in safety and in cost when compared with rechargeable lithium batteries [10]. However, memory effect, which is the temporary reduction of the capacity of a cell after repetitive shallow charge-discharge cycles, may be observed in metal hydride-nickel hydroxide cells as well as in nickel-cadmium cells. Although the cause of memory effect is still unclear, it is most likely due to morphological changes in nickel hydride electrodes [11].

$\leftarrow e \rightarrow$

M	$\leftrightarrow H_2O \leftrightarrow$	NiOOH
$\updownarrow$		$\updownarrow$
MH		$Ni(OH)_2$

$\leftrightarrow OH^- \leftrightarrow$

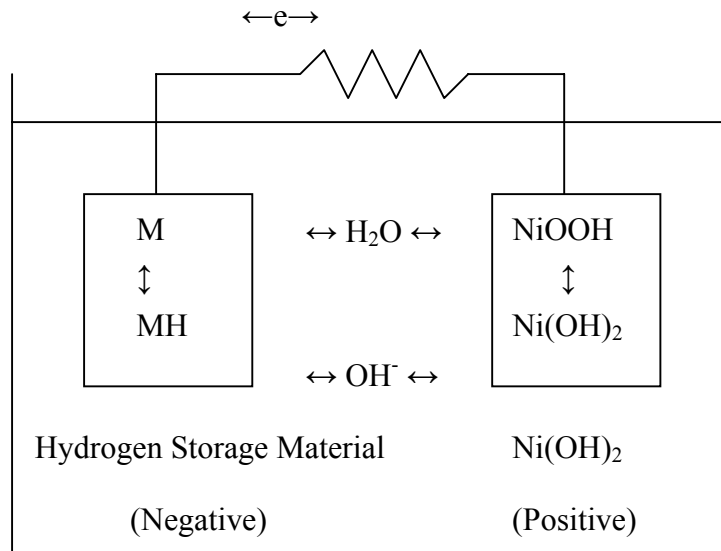Hydrogen Storage Material $Ni(OH)_2$

(Negative)   (Positive)

Figure 3. A schematic of the secondary battery with hydrogen storage materials.

Hydrogen storage materials may be used as hydrogen purifiers. Since hydrogen storage materials selectively absorb and desorb hydrogen, highly purified hydrogen can be derived from crude gas. Crude gas is introduced into the system filled with hydrogen storage materials, and hydrogen start reacting with them as shown in Figure 4 (a). The system is cooled so that the hydrogen storage material can absorb hydrogen. Impurity is evacuated from the system and only pure hydrogen is left in the form of a hydride as shown in Figure 4 (b). This method has an advantage in running costs when compared with the conventional gas method. The conventional method makes use of the difference in boiling points of hydrogen (20 K) and other gases, i.e. methane (90 K), which needs much energy for cooling. On the other hand, hydrogen storage materials can absorb and purify hydrogen at ambient temperature. Moreover, when the purification is finished, the product, hydrogen, is already absorbed into the hydrogen storage material. Therefore, there is no expense for compression [12].

○ Hydrogen ● Impurity Gas (MH) Metal Hydride (M) Metal
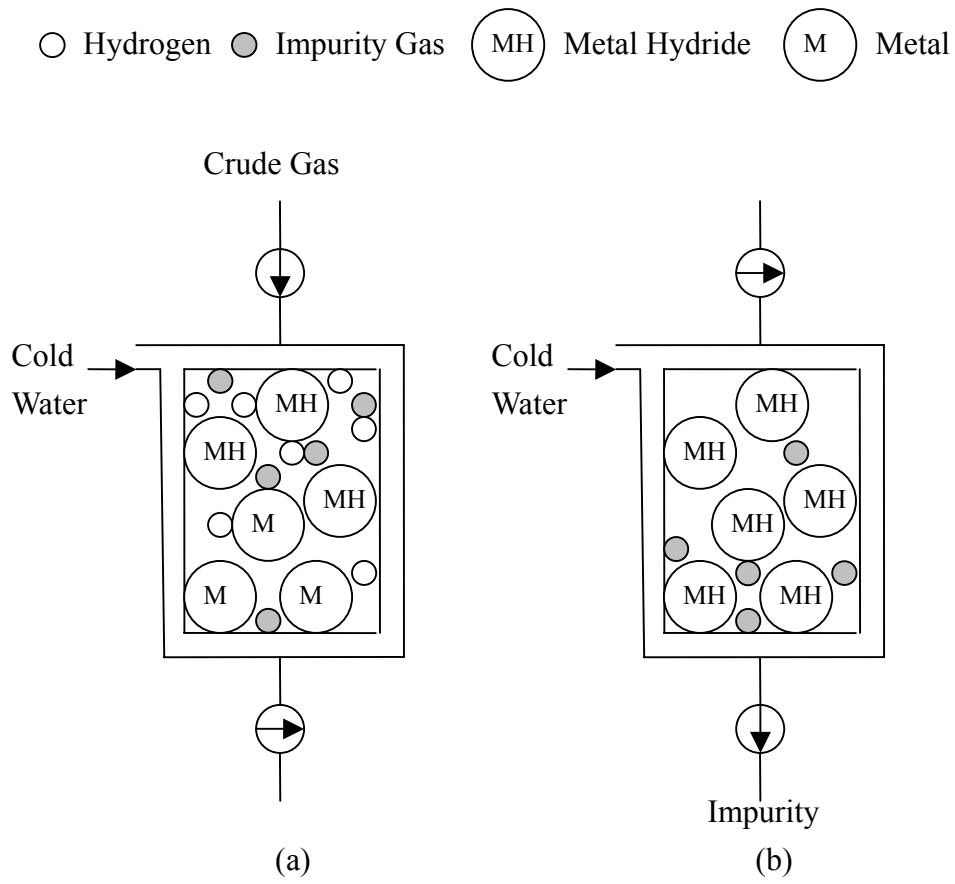
Figure 4. A schematic of hydrogen purifier.

1.2 Historical Review

Conventional Hydrogen Storage Materials

Hydrogen atom is so small that it can easily enter the interstitial voids and form M-H bonds in many metals, such as titanium, zirconium, vanadium, or rare-earth metals. However, the formed hydrides are often so stable that hydrogen can not be easily released, which is a critical issue for storing hydrogen. On the other hand, there are some metals that do not form stable hydrides, such as iron or nickel. It is quite intuitive that when the metal which forms stable hydrides is mixed with the metal which does not form stable hydrides, the alloy can absorb and desorb hydrogen relatively easily. These alloys are called hydrogen storage materials.

One of the conventional hydrogen storage materials is Mg_2Ni which was discovered in 1968 at Brookhaven National Laboratory, USA. This material can absorb and desorb hydrogen as much as 4 H/Mg_2Ni. However, it cannot absorb and desorb hydrogen near room temperature. It needs to be heated up to 250^oC. Shortly thereafter, $LaNi_5$ was discovered in 1970 at Philips Research Laboratories, the Netherlands. This material can absorb and desorb as much as 6 $H/LaNi_5$ at room temperature. $MmNi_5$-based materials in which Mm (mischmetal) replaces La because of its lower cost and better performance are in common use today. In 1974, TiFe which absorbs as much as 1.95 H/TiFe was discovered at Brookhaven National Laboratory, USA. Subsequently, Mg-, Ti-, and Mm-based materials were modified by replacing some atoms with other transition metals for their application to products. Some common hydrogen storage materials are compared in Table. 1.

Table.1 Hydrogen content of various storage media (Reproduced from [13])

Media	Density (g/ml)	H$_2$ content (Wt.% H$_2$)	Volumetric H density (10^{22} atoms H/ml)
H$_2$, liquid (20 K)	0.071	100.0	4.2
H$_2$, gas at 100 atm.	8.2 × 10^{-5}	100.0	0.5
NH$_3$, liquid	0.60	17.7	6.5
CaH$_2$	1.80	4.8	5.1
MgH$_2$	1.40	7.6	6.7
ZrH$_2$	5.60	2.2	7.3
TiH$_2$	3.80	4.0	9.1
VH$_2$	4.50	2.1	11.4
Mg$_2$NiH$_{4.2}$	2.60	3.8	5.9
LaNi$_5$H$_{6.7}$	8.25	1.5	7.6

Since many hydrogen storage materials have high volumetric hydrogen density, they are suitable for use in a stationary storage system. However, since weight fraction of hydrogen in metal hydrides is much lower than that of liquid hydrogen, metal hydrides have a disadvantage when they are used in a mobile storage system. For example, fueled with 200kg of ~2 wt% H$_2$ hydrogen storage material (TiFe) and powered by a 44 kW motor, the car can run only about 150 km, which is far below a practical level of ~ 500 km [14]. Therefore, advanced materials with high weight fraction of hydrogen in solid state are required.

Alkali Metal Aluminohydrides

The alkali metal aluminohydrides, such as $LiAlH_4$, $NaAlH_4$, $Mg(AlH_4)_2$, $LiMg(AlH_4)_3$, and $LiMg_3(AlH_4)_7$ contain as much as 10.5, 7.4, 9.3, 9.7, and 9.5 wt.% hydrogen, respectively, while the conventional hydrogen storage materials such as $LaNi_5$ and TiFe can store only 1.4 and 1.8 wt.% H_2, respectively. However, once the alkali metal aluminohydrides desorb hydrogen, they do not absorb it again below 100 atm H_2. In other words, pure alkali metal aluminohydrides are irreversible hydrogen storage materials. Furthermore, alkali metal compounds are quite unstable when heated above their melting points. These problems make it difficult to apply complex aluminohydrides to practical hydrogen storage materials [15].

Recently Bogdanovic et al. succeeded in re-hydrogenation of $NaAlH_4$ below 100 atm H_2 by doping it with Ti and Fe organo-metallic compounds [1, 2]. This revived the possibility of applying alkali metal aluminohydrides to practical hydrogen storage, especially the lithium compounds, because of their highest hydrogen content per unit mass within the series of alkali metal aluminohydrides.

The thermal properties of $LiAlH_4$ have been examined extensively by Dilts and Ashby [16], and recently Dymova et al. [17-18] refined the details about its multiple step decomposition process by pointing out a melting step prior to its decomposition.

$$LiAlH_4(S) \rightarrow LiAlH_4(L) \qquad\qquad (endo, 165\text{-}180^oC) \quad (1.1)$$

$$LiAlH_4(L) \rightarrow 1/3Li_3AlH_6(S) + 2/3Al(S) + H_2(G) \qquad (exo, 170\text{-}220^oC) \quad (1.2)$$

$$Li_3AlH_6(S) \rightarrow 3LiH(S) + Al(S) + 1.5H_2(G) \qquad (endo, 220\text{-}275^oC) \quad (1.3)$$

$$LiH(S) + Al(S) \rightarrow AlLi(S) + 1/2H_2(G) \qquad (endo, 575\text{-}605^oC) \quad (1.4)$$
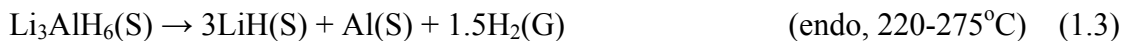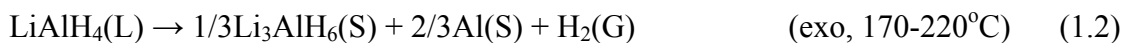
By the end of the third stage, the total amount of desorbed hydrogen is 7.9 wt%, which would be an unusually high value if this material was a reversible hydrogen storage material. Since the last reaction (equation 1.4) takes place at high temperature, its use would be impractical.

Dymova et al. [17, 18] also showed that the high decomposition temperature of $LiAlH_4$

is due to kinetic constraints and not due to thermodynamic limitations because the free energy change corresponding to the decomposition (1.2) is negative. Thus, $LiAlH_4$ decomposes only after the kinetic constraints are relieved by melting. This kinetic problem, or the activation energy, raises the decomposition temperature and thus causes high equilibrium pressure during re-hydrogenation.

Recently, Balema et al. [19] succeeded in carrying out a solid state transformation of $LiAlH_4$ into Li_3AlH_6 without its heating by doping it with $TiCl_4$ followed by a short ball-milling. This decreases the decomposition temperature.

1.3 Statement of Work

In this research $(Zr_{27}Ti_9)(Ni_{38}V_5Mn_{16}Cr_5)$, $La(Ni_{4.85}Sn_{0.15})$, Al_3Ti, and $PdCl_2$ were examined as catalysts to reduce the decomposition temperature and the equilibrium hydrogen pressure of $LiAlH_4$, and thus to improve hydrogen absorption and desorption properties of $LiAlH_4$ as a reversible hydrogen storage material.

2. EXPERIMENTAL PROCEDURE

2.1 Sample Preparation and hydrogen absorption/desorption

$LiAlH_4$ (> 98 wt.% pure) was purchased from Sigma-Aldrich, and all operations on this material were carried out in a helium atmosphere in a glove box. Gas atomized $Zr_{27}Ti_9Ni_{38}V_5Mn_{16}Cr_5$ and $LaNi_{4.85}Sn_{0.15}$ powders were obtained from the Materials Preparation Center at the Ames Laboratory. Since the phase composition of gas atomized $LaNi_{4.85}Sn_{0.15}$ was affected by varying Ni:Sn ratio during rapid solidification, the powder was annealed in an evacuated quartz tube at 950 ^{o}C for 6 hours. Al_3Ti was prepared by arc melting of stoichiometric mixture of Al (99.999 wt.%) purchased from Alfa Aesar and Ti (99.99 wt.%) received from TIMET. The sample during arc melting was turned over 6 times to ensure homogeneity. $PdCl_2$ (99 wt.% pure) was purchased from Sigma-Aldrich.

$LiAlH_4$ was ball-milled with the conventional hydrogen storage materials, $LaNi_{4.85}Sn_{0.15}$ and $Zr_{27}Ti_9Ni_{38}V_5Mn_{16}Cr_5$, at the volume ratio of 1:1 for 1 and 6 hours for each sample, and also with 3 mol% of Al_3Ti, and $PdCl_2$ for 7 hours. A Spex-8000 mill, a hardened-steel vial, and steel balls (21g) were used for the ball-milling. The hardened-steel vial was sealed under helium and was air-cooled to prevent its heating during ball-milling. After the ball-milling, the samples were extracted in the glove box, the vial was cleaned by sand-bluster using alumina powder and the steel balls were disposed of.

The ball-milled samples were heated to 300 ^{o}C so that $LiAlH_4$ and Li_3AlH_6 decompose into LiH, Al, and H_2 completely. Figure 5 illustrates the equipment used for heating and hydrogenating samples.

After the sample decomposed, hydrogen was introduced into the sample at room temperature at about 3 atm. pressure, or at the elevated temperature at about 70 atm. pressure. As for the experiments with lower hydrogen pressure (Figure 5), absorbed hydrogen content was determined by measuring the difference of hydrogen pressure before and after the completion of

absorption using known volume of the equipment. As for the experiments with higher pressure, absorbed hydrogen content was not measured because the equipment was not designed to measure the amount of hydrogen absorbed at high pressure.
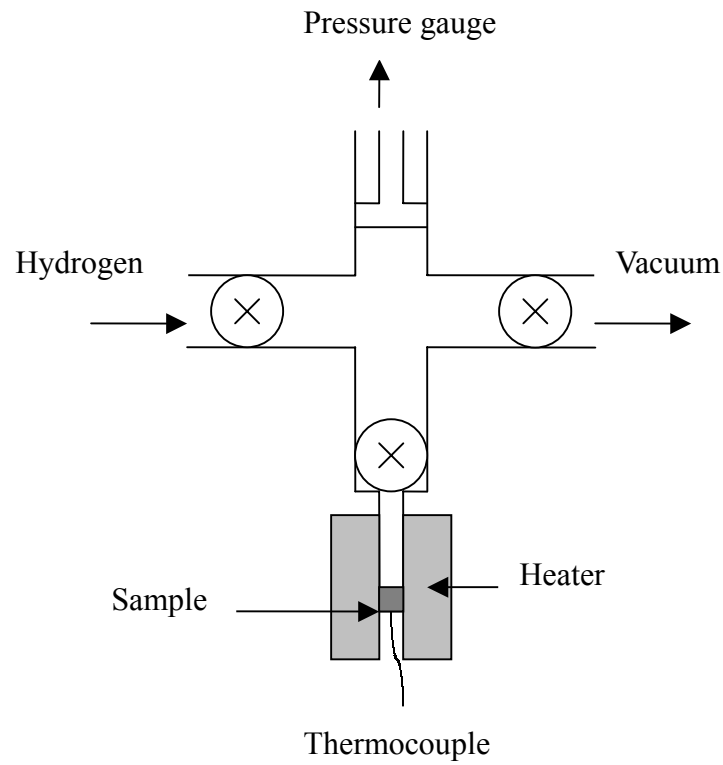
Figure 5. A schematic of the low pressure equipment for heating and hydrogenating samples.

2.2 Sample Characterizations

X-ray powder diffraction (XRD) measurements were conducted using a Scintag powder diffractometer with CuK$_\alpha$ radiation to determine phase content and to establish changes of sample structure. When possible, XRD patterns of the various materials were analyzed using the Rietveld method.

Differential thermal analysis (DTA) measurements to determine the thermal properties of the samples and identify the reactions were conducted using Perkin Elmer DTA 7 unit from 20 to 300 ^{o}C with a heating rate of 10 ^{o}C/min in an argon atmosphere. Alumina crucibles were used as holders, and aluminum oxide was used as a reference material.

Scanning electron microscopy (SEM) was used to study the morphology of the particles. Secondary-electron imaging was used to establish particle surface and to explain hydrogen absorption properties. R. J. Lee Instruments, Ltd. personal SEM was used for these measurements.

3. DATA ANALYSES

3.1 LiAlH$_4$ + Zr$_{27}$Ti$_9$Ni$_{38}$V$_5$Mn$_{16}$Cr$_5$

3.1.1 After 1 Hour Ball-milling

Figure 6 shows the result of the XRD measurement of the as gas atomized Zr$_{27}$Ti$_9$Ni$_{38}$V$_5$Mn$_{16}$Cr$_5$. The powder contains two main phases, C14 and C15, where C14 is hexagonal phase and C15 is cubic phase. The lattice parameters were determined to be a=4.97150 (1) Å, c=8.11082 (2) Å for the C14 phase and a=7.0265 (3) Å for the C15 phase, where the numerals in the parentheses are the standard deviations in the last significant digits. The powder diffraction pattern is consistent with the previous study by Z. Shi [20].

Figure 7 shows the results of the XRD measurements of pure Zr$_{27}$Ti$_9$Ni$_{38}$V$_5$Mn$_{16}$Cr$_5$ ball-milled for 1 hour, ball-milled for 1 hour and then heated to 300 ^{o}C for 15 min, and ball-milled for 1 hour, heated to 300 ^{o}C for 15 min, and then hydrogenated. After ball-milling for 1 hour, Bragg peaks broaden, which indicates that the sample particles are broken into small pieces and are partially amorphized. After heating to 300 ^{o}C for 15 min, the peaks corresponding to two phases found in Zr$_{27}$Ti$_9$Ni$_{38}$V$_5$Mn$_{16}$Cr$_5$ become slightly sharper because of stress relief and relaxation of the structure. After hydrogenation, the peaks of Zr$_{27}$Ti$_9$Ni$_{38}$V$_5$Mn$_{16}$Cr$_5$ shift to lower Bragg angles. This is expected when hydrogen enters the interstitial sites of Zr$_{27}$Ti$_9$Ni$_{38}$V$_5$Mn$_{16}$Cr$_5$, thus expanding the lattice.
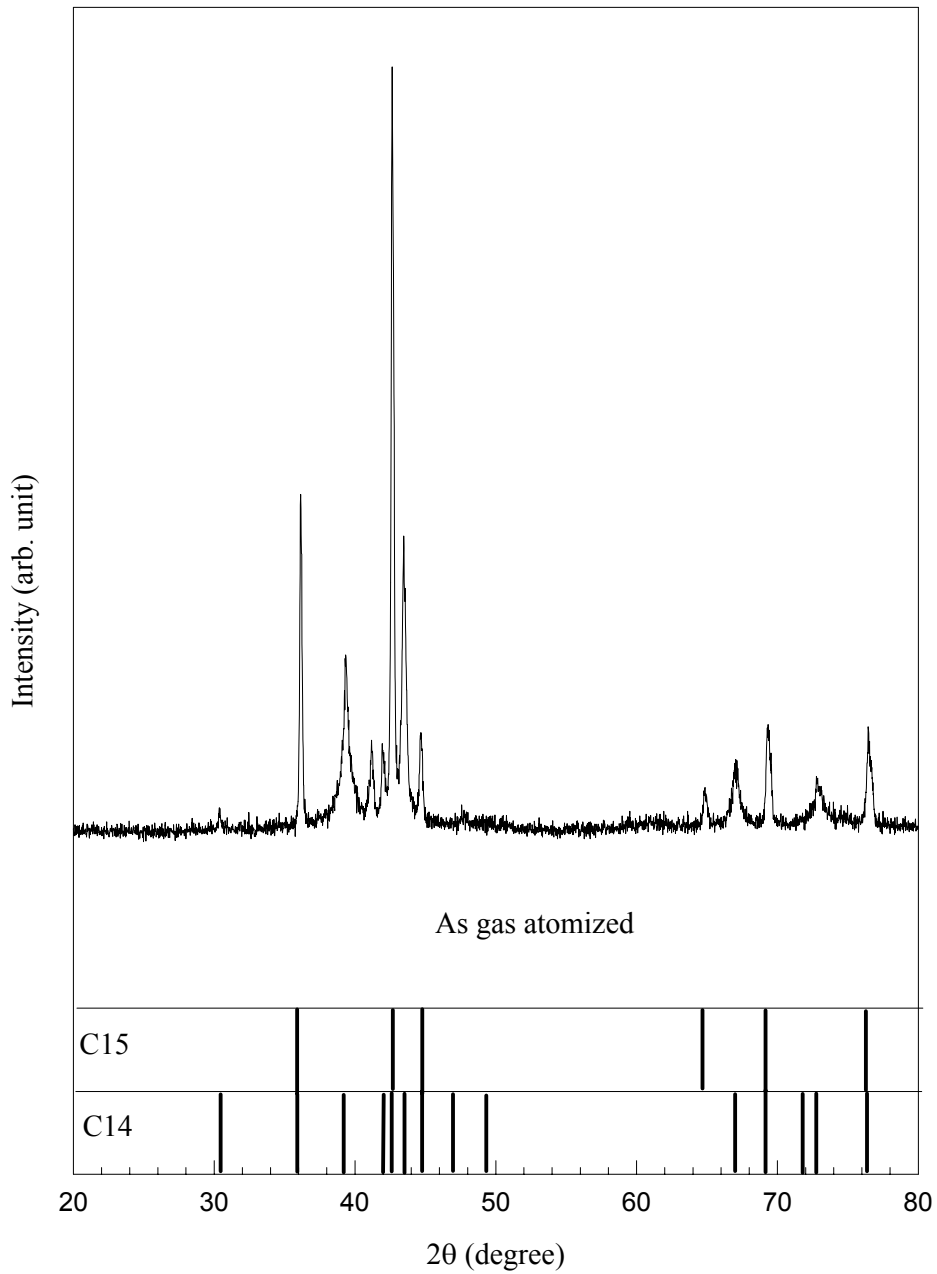
Figure 6. The XRD pattern of gas atomized $Zr_{27}Ti_9Ni_{38}V_5Mn_{16}Cr_5$ powder. Vertical bars at the bottom indicate calculated Bragg peak positions of corresponding phases.

18
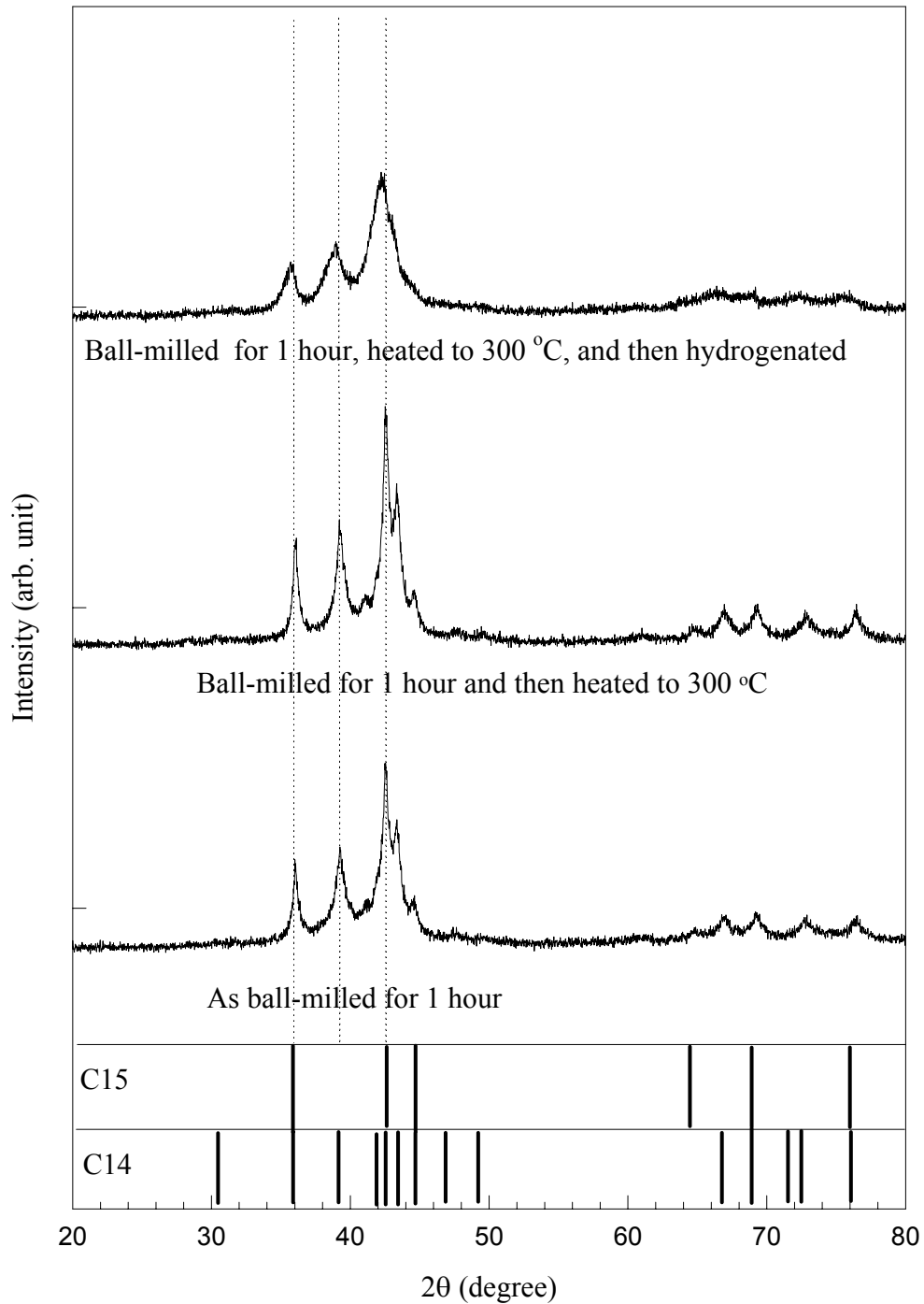
Figure 7. The XRD patterns of pure $Zr_{27}Ti_9Ni_{38}V_5Mn_{16}Cr_5$ ball-milled for 1 hour, ball-milled for 1 hour and then heated to 300 ^{o}C for 15 min, and ball-milled for 1 hour, heated to 300 ^{o}C, and then hydrogenated.
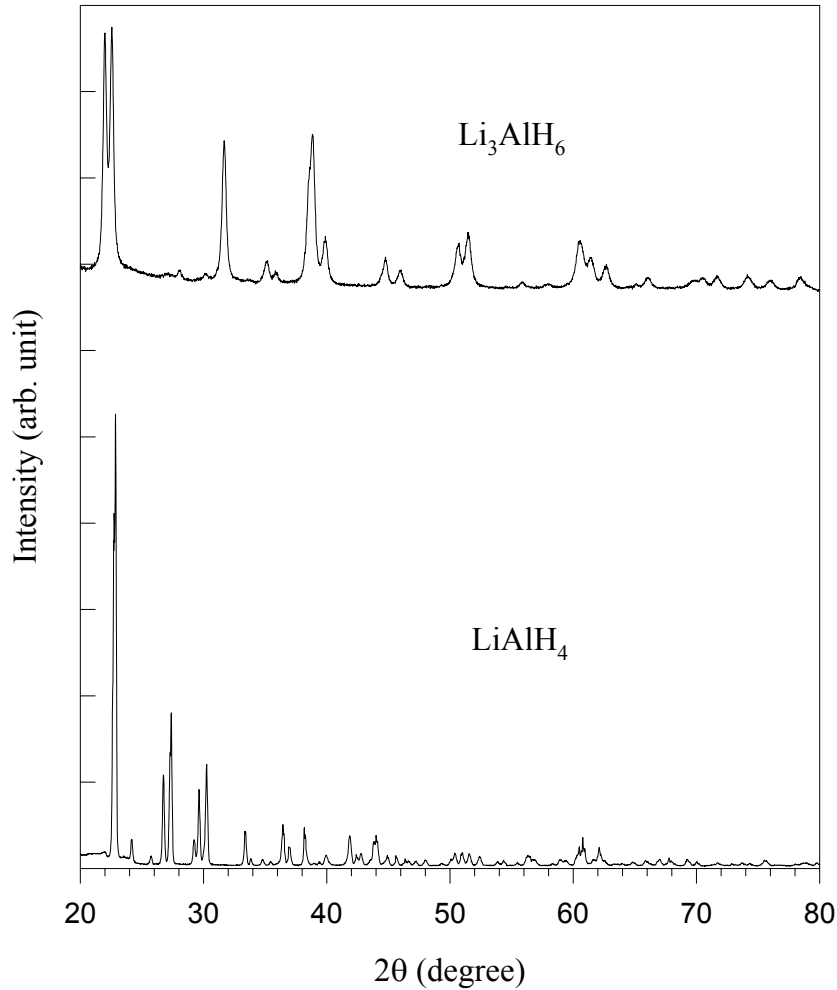
Figure 8 shows the results of the XRD measurements of $LiAlH_4 + Zr_{27}Ti_9Ni_{38}V_5Mn_{16}Cr_5$ taken in 1:1 volume ratio ball-milled for 1 hour, ball-milled for 1 hour and then held at 300 ^{o}C for 15 min, and ball-milled for 1 hour, heated to 300 ^{o}C, and then hydrogenated.

After 1-hour ball-milling, no peaks of $LiAlH_4$ or Li_3AlH_6 (See Figure 9 [21]) are found. Instead, the peaks corresponding to Al are found. This indicates that $LiAlH_4$ decomposes into Li_3AlH_6, Al, and H_2 during ball-milling.

After heating to 300 ^{o}C and holding at this temperature for 15 min, the peaks corresponding to $Zr_{27}Ti_9Ni_{38}V_5Mn_{16}Cr_5$ in the specimen become sharper than those of pure $Zr_{27}Ti_9Ni_{38}V_5Mn_{16}Cr_5$ ball-milled for 1 hour and heated to 300 ^{o}C. This indicates that the particles of $Zr_{27}Ti_9Ni_{38}V_5Mn_{16}Cr_5$ in the specimen ball-milled with $LiAlH_4$ are somewhat larger sizes.

Hydrogenation at 3 atm. pressure at room temperature has no effect on the phase composition of this sample. However, the peaks of pure $Zr_{27}Ti_9Ni_{38}V_5Mn_{16}Cr_5$ ball-milled for 1 hour, heated to 300 ^{o}C for 15 min and then hydrogenated, shift to lower Bragg angles as was discussed earlier. This can be because of a lack of the activation, which means that in this case $LiAlH_4$ works as a shock absorber during ball-milling and some particle surfaces remain intact. The XRD measurements could not identify any zirconium oxides, ZrO_x, because the Bragg peak positions corresponding to ZrO_x are similar to those of $Zr_{27}Ti_9Ni_{38}V_5Mn_{16}Cr_5$ and because the amount of ZrO_x is presumably small. However, it is well established that the particle surface of the samples containing elements such as Al, La, Mg, Ti, or Zr is easily poisoned by their oxides and hydroxides, and they prevent hydrogen from entering the inside of the particles.
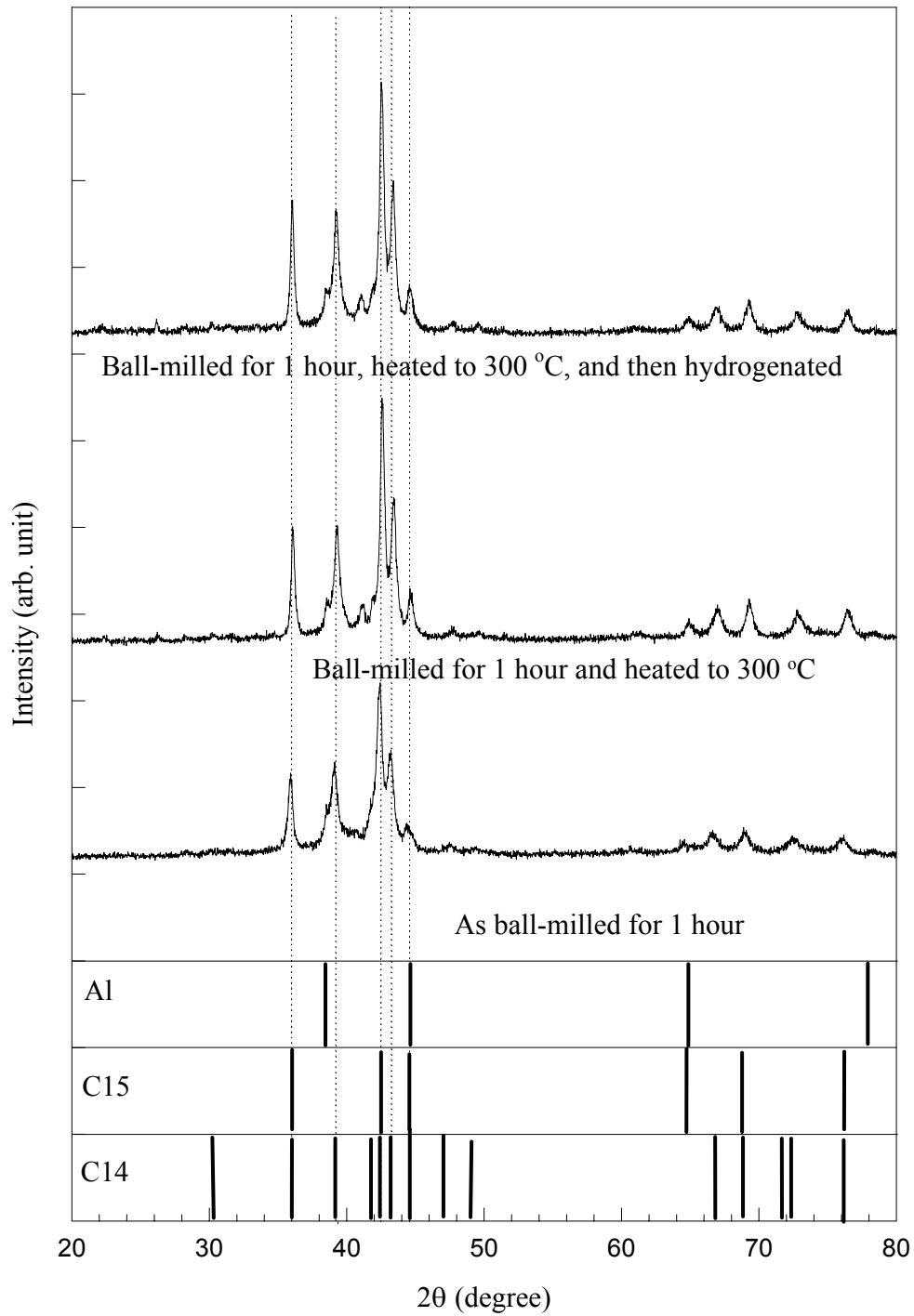
Figure 8. The XRD patterns of LiAlH$_4$ + Zr$_{27}$Ti$_9$Ni$_{38}$V$_5$Mn$_{16}$Cr$_5$ taken in 1:1 volume ratio and ball-milled for 1 hour, ball-milled for 1 hour and then heated to 300 ^{o}C for 15 min, and ball-milled for 1 hour, heated to 300 ^{o}C, and then hydrogenated.
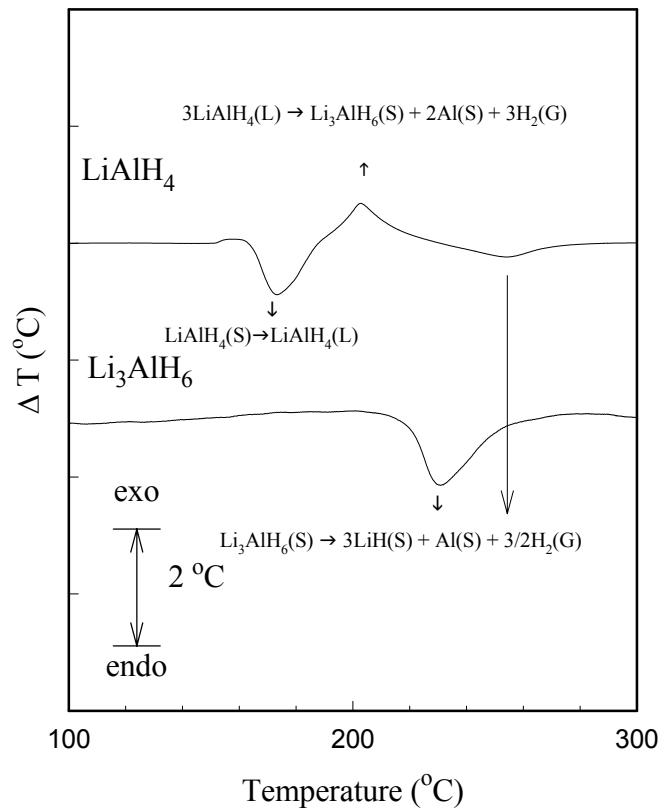
Figure 9. XRD patterns of LiAlH$_4$ and Li$_3$AlH$_6$ [21].

Figure 10 shows the results of the DTA measurements of pure Zr$_{27}$Ti$_9$Ni$_{38}$V$_5$Mn$_{16}$Cr$_5$ ball-milled for 1 hour, ball-milled for 1 hour and then heated to 300 $^{\circ}$C and held at this temperature for 15 min, and ball-milled for 1 hour, heated to 300 $^{\circ}$C, and then hydrogenated. No anomalies are found either after ball-milling for 1 hour or after heating to 300 $^{\circ}$C for 15 min. This means that there is no crystallization between 100 and 300 $^{\circ}$C, and any anomalies of DTA traces of LiAlH$_4$ + Zr$_{27}$Ti$_9$Ni$_{38}$V$_5$Mn$_{16}$Cr$_5$ after ball-milling will not be due to the crystallization of amorphous phases. After hydrogenation, a broad DTA peak is found between 100 $^{\circ}$C and 270 $^{\circ}$C,

which is associated with hydrogen evolution from $Zr_{27}Ti_9Ni_{38}V_5Mn_{16}Cr_5H_x$.
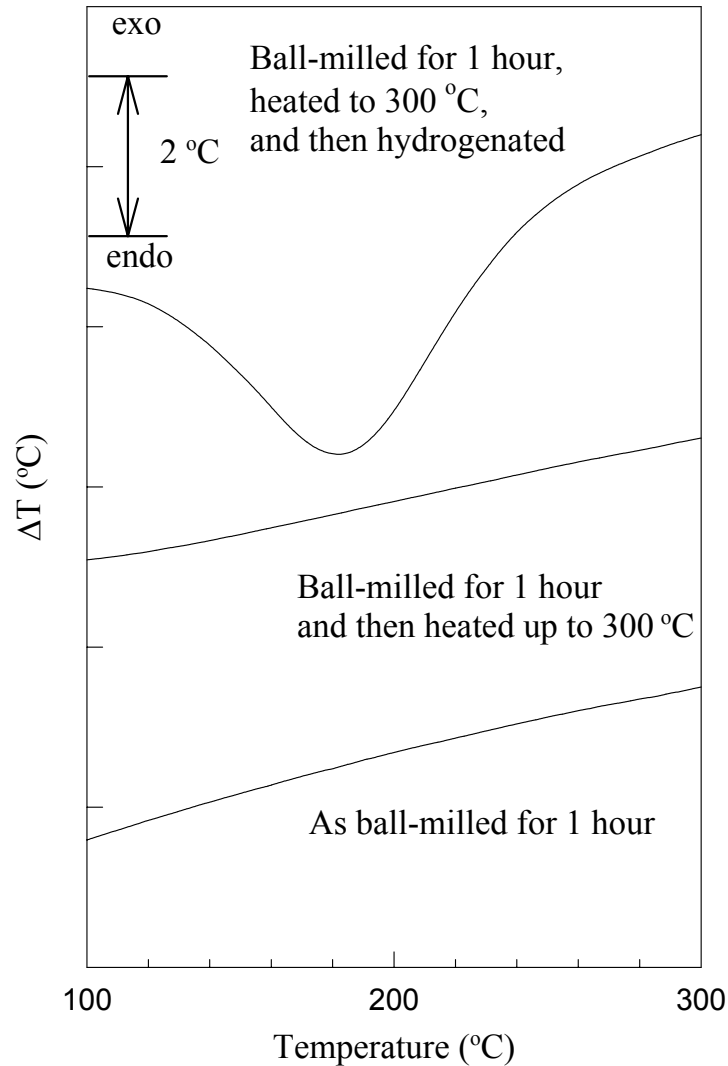
Figure 10. The DTA traces of pure $Zr_{27}Ti_9Ni_{38}V_5Mn_{16}Cr_5$ ball-milled for 1 hour, ball-milled for 1 hour and then heated to 300 $^{\circ}$C for 15 min, and ball-milled for 1 hour, heated to 300 $^{\circ}$C, and then hydrogenated.

Figure 11 shows the results of the DTA measurements of $LiAlH_4$ + $Zr_{27}Ti_9Ni_{38}V_5Mn_{16}Cr_5$ taken in 1:1 volume ratio and ball-milled for 1 hour, ball-milled for 1 hour and then heated to 300 $^{\circ}$C and held at this temperature for 15 min, and ball-milled for 1 hour, heated to 300 $^{\circ}$C, and then hydrogenated. The anomalies observed in the sample ball-milled for 1 hour are similar to those of pure $LiAlH_4$ (See Figure 12 [21]), except for the peak corresponding

to the melting of LiAlH$_4$ (160-190 $^{\circ}$C). All peaks shift to lower temperature by about 30 $^{\circ}$C when compared to the corresponding peaks of pure LiAlH$_4$. This means that Zr$_{27}$Ti$_9$Ni$_{38}$V$_5$Mn$_{16}$Cr$_5$ works as a reasonably good catalyst of the decomposition of LiAlH$_4$. No anomalies are found after hydrogenation at 3 atm. pressure at room temperature. This means that Zr$_{27}$Ti$_9$Ni$_{38}$V$_5$Mn$_{16}$Cr$_5$ does not work as a catalyst in the reverse reaction at these very mild conditions.
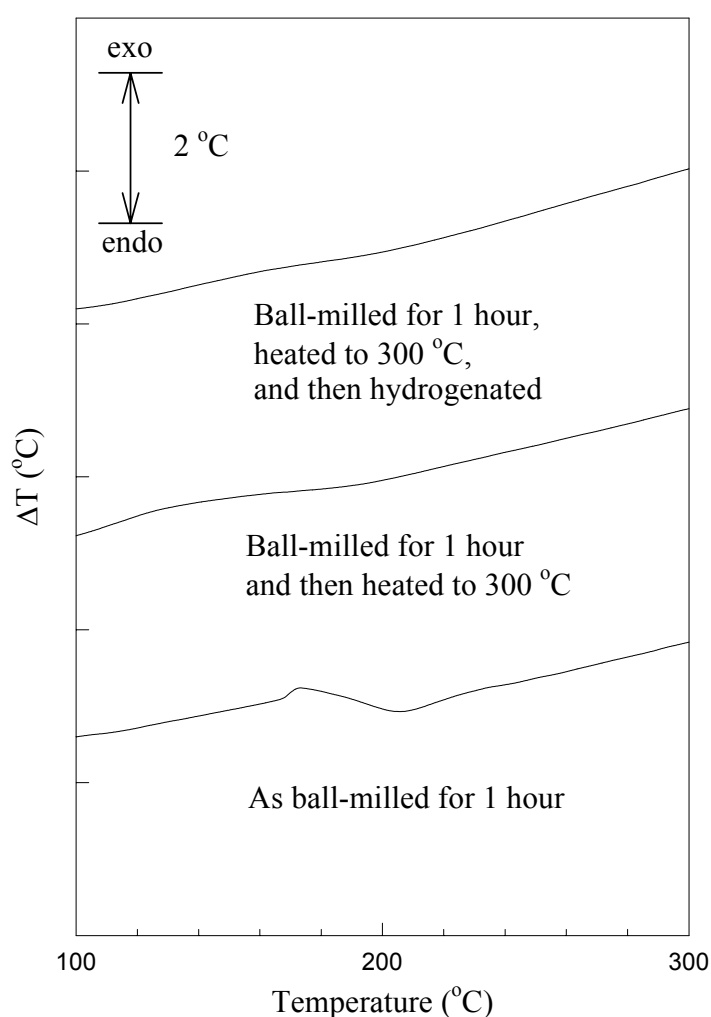
Figure 11. The DTA traces of LiAlH$_4$ + Zr$_{27}$Ti$_9$Ni$_{38}$V$_5$Mn$_{16}$Cr$_5$ taken in 1:1 volume ratio and ball-milled for 1 hour, ball-milled for 1 hour and then heated to 300 $^{\circ}$C for 15 min, and ball-milled for 1 hour, heated to 300 $^{\circ}$C, and then hydrogenated.

Figure 12. The DTA traces of $LiAlH_4$ and Li_3AlH_6 [21].

Figure 13 shows hydrogenation behavior of $Zr_{27}Ti_9Ni_{38}V_5Mn_{16}Cr_5$ ball-milled for 1 hour. After three cycles of hydrogenation and dehydrogenation the sample appears to be fully activated and absorbed about 0.7 wt.% H_2. The amorphous phases seem to be the cause of relatively low hydrogen capacity, when compared to that of the crystalline $Ti_{0.2}Zr_{0.8}Ni_{1.3}Mn_{0.5}V_{0.2}$ sample, which is about 1.5 wt.% H_2 at 3 atm. pressure at 30 °C [22].

Figure 14 shows hydrogenation behavior of $LiAlH_4 + Zr_{27}Ti_9Ni_{38}V_5Mn_{16}Cr_5$ taken in 1:1 volume ratio and ball-milled for 1 hour. The mixture absorbed only about 0.05 wt.% H_2. This can be because some particles were inactive as discussed above.
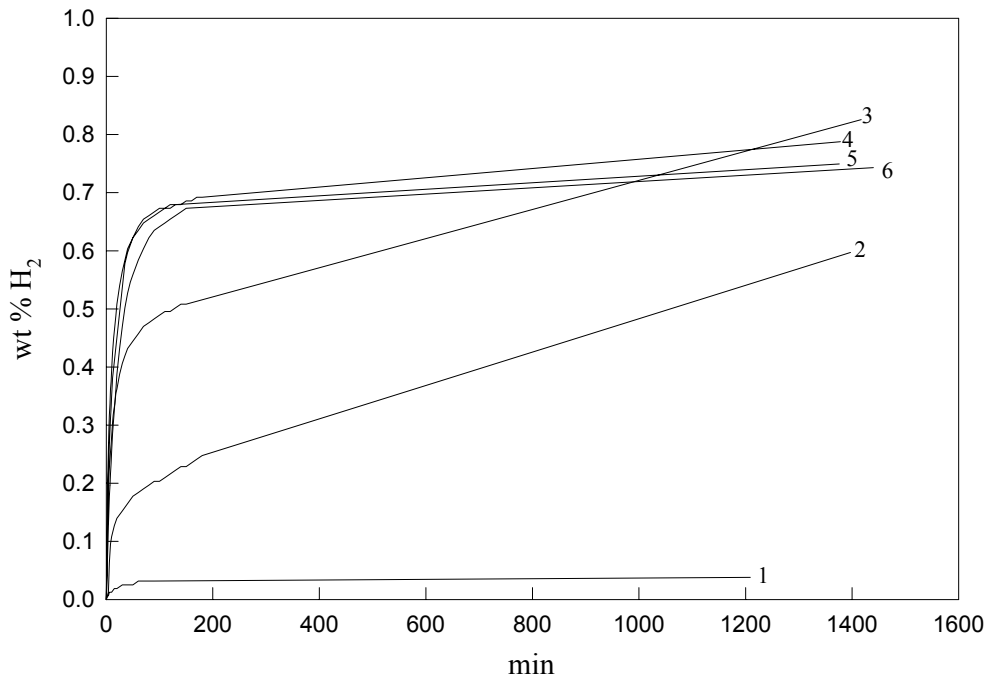
Figure 13. Hydrogenation behavior of pure $Zr_{27}Ti_9Ni_{38}V_5Mn_{16}Cr_5$ at 3.4-2.5 atm pressure at room temperature after ball-milling for 1 hour. The numeral next to the curve indicates hydrogenation cycle number.
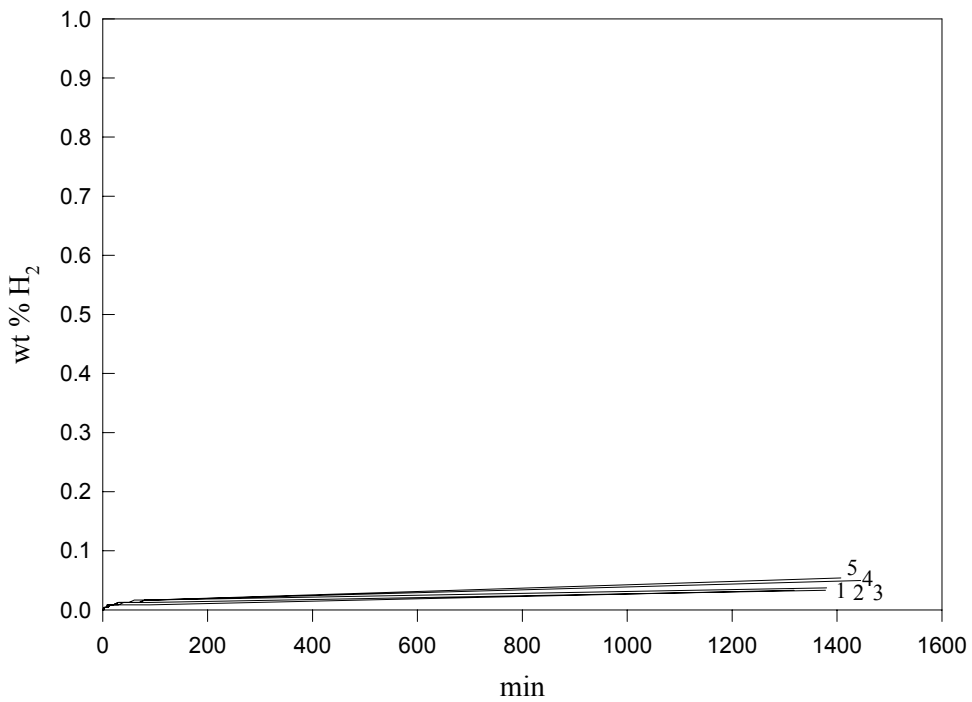
Figure 14. Hydrogenation behavior of $LiAlH_4 + Zr_{27}Ti_9Ni_{38}V_5Mn_{16}Cr_5$ at 3.4-3.3 atm pressure at room temperature taken in 1:1 volume ratio and ball-milled for 1 hour. The numeral next to the curve indicates hydrogenation cycle number.

Figure 15 shows the morphology of the sample particles of gas atomized $Zr_{27}Ti_9Ni_{38}V_5Mn_{16}Cr_5$. The shapes are spherical and the sizes of the particles vary from 2 to 35 μm.

Figure 16 shows the morphology of the particles of $Zr_{27}Ti_9Ni_{38}V_5Mn_{16}Cr_5$ ball-milled for 1 hour. The particles are broken into pieces varying from less than 1 to 25 μm. The small particles under 1 μm agglomerate, which is consistent with peak broadening in the XRD results (See Figure 7).

Figure 17 shows the morphology of the particles of $LiAlH_4$ + $Zr_{27}Ti_9Ni_{38}V_5Mn_{16}Cr_5$ taken in 1:1 volume ratio and ball-milled for 1 hour. The particles are agglomerated and the sizes are distributed from less than 1 to 25 μm. Surprisingly, some spherical particles remain, which supports earlier assumption that $LiAlH_4$ works as a shock absorber, and that a lack of the activation on this specimen is possible. This feature also explains the sharp Bragg peaks in the XRD results (See Figure 8). It looks that there are many tiny particles of $Zr_{27}Ti_9Ni_{38}V_5Mn_{16}Cr_5$. However, most of them are probably the particles of $LiAlH_4$ which are originally small, because the spherical particles of $Zr_{27}Ti_9Ni_{38}V_5Mn_{16}Cr_5$ with about 5 μm diameter are not broken. Moreover, if particle sizes become larger, total surface area of the particles become smaller. Therefore, the smaller total particle surface area of $Zr_{27}Ti_9Ni_{38}V_5Mn_{16}Cr_5$ in the sample ball-milled with $LiAlH_4$ may be the reason of its inferior hydrogen absorption properties when compared to that in pure $Zr_{27}Ti_9Ni_{38}V_5Mn_{16}Cr_5$ sample in addition to a lack of the activation.
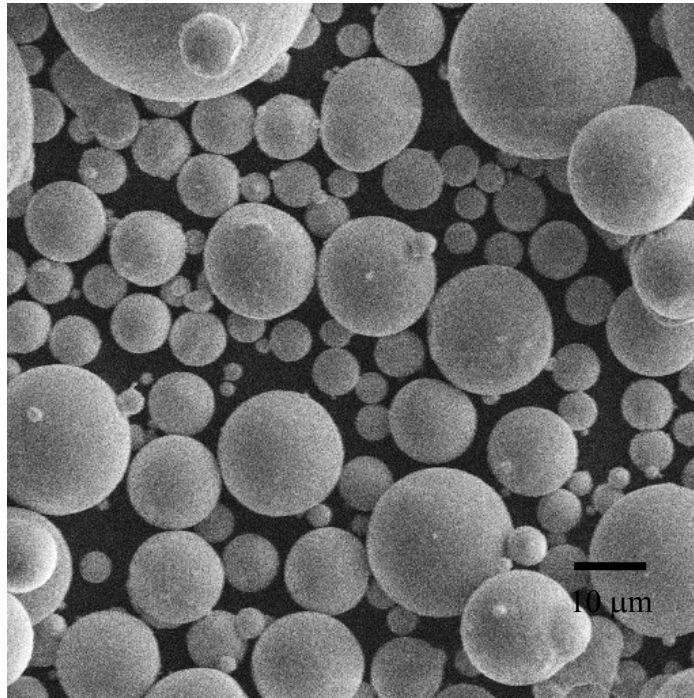
Figure 15. Morphology of gas atomized $Zr_{27}Ti_9Ni_{38}V_5Mn_{16}Cr_5$ (x 1000).
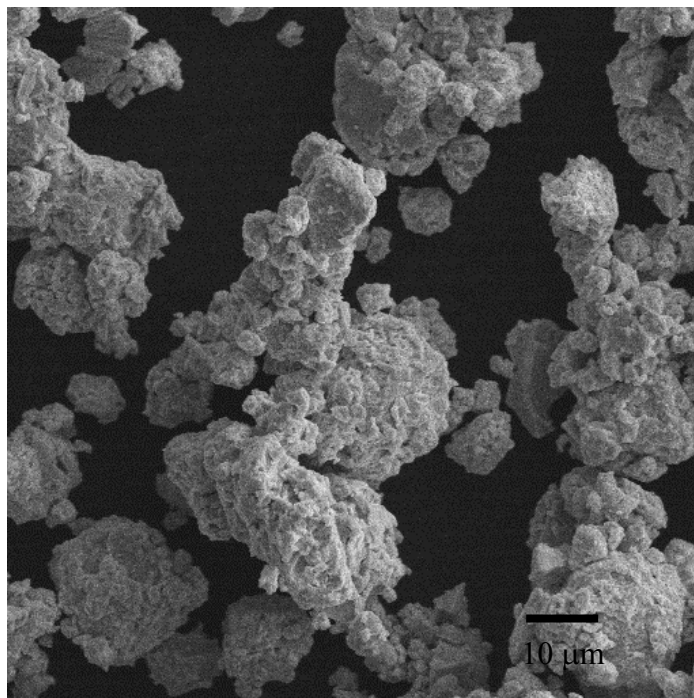
Figure 16. Morphology of pure $Zr_{27}Ti_9Ni_{38}V_5Mn_{16}Cr_5$ ball-milled for 1 hour (x 1000).
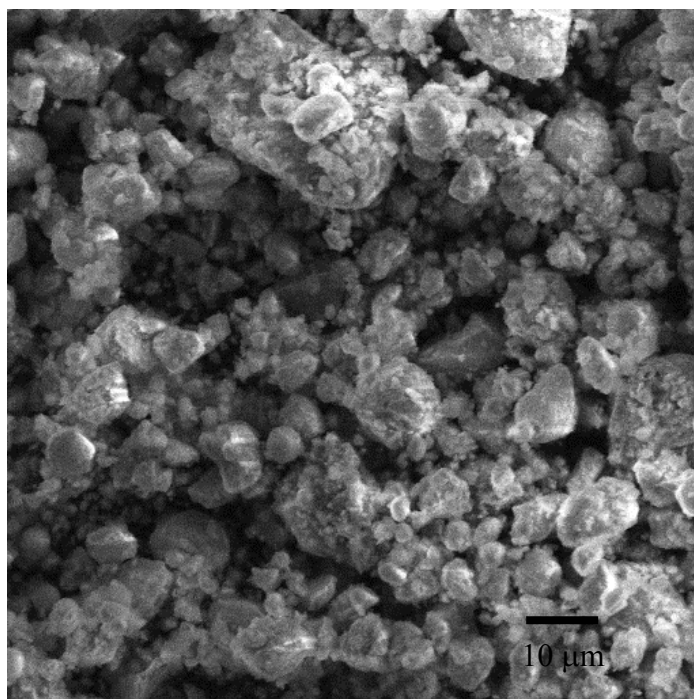
Figure 17. Morphology of LiAlH$_4$ + Zr$_{27}$Ti$_9$Ni$_{38}$V$_5$Mn$_{16}$Cr$_5$ taken in 1:1 volume ratio and ball-milled for 1 hour (x 1000).

3.1.2 After 6 Hours Ball-milling

Figure 18 shows the results of the XRD measurements of pure $Zr_{27}Ti_9Ni_{38}V_5Mn_{16}Cr_5$ ball-milled for 6 hours, ball-milled for 6 hours and then heated to 300 ^{o}C and held at this temperature for 15 min, and ball-milled for 6 hours, heated to 300 ^{o}C, and then hydrogenated. After ball-milling for 6 hours, Bragg peaks become broader than those of $Zr_{27}Ti_9Ni_{38}V_5Mn_{16}Cr_5$ ball-milled for 1 hour (See Figure 7). This seems to be the result of a larger fraction of an amorphous phase, and not because the particle sizes of $Zr_{27}Ti_9Ni_{38}V_5Mn_{16}Cr_5$ ball-milled for 6 hours become smaller than those of $Zr_{27}Ti_9Ni_{38}V_5Mn_{16}Cr_5$ ball-milled for 1 hour (See SEM data, Figure 24). This will be further discussed when comparing the results of hydrogenation behavior and also SEM micrograms. After heating to 300 ^{o}C, the Bragg peaks become sharper because of the stress relief and the relaxation of the structure. After hydrogenation, Bragg peaks of $Zr_{27}Ti_9Ni_{38}V_5Mn_{16}Cr_5$ broaden. However, unlike $Zr_{27}Ti_9Ni_{38}V_5Mn_{16}Cr_5$ ball-milled for 1 hour, Bragg peaks do not shift to lower angles (See Figure 7). This is because the amount of the absorbed hydrogen is small as quantitatively shown later.
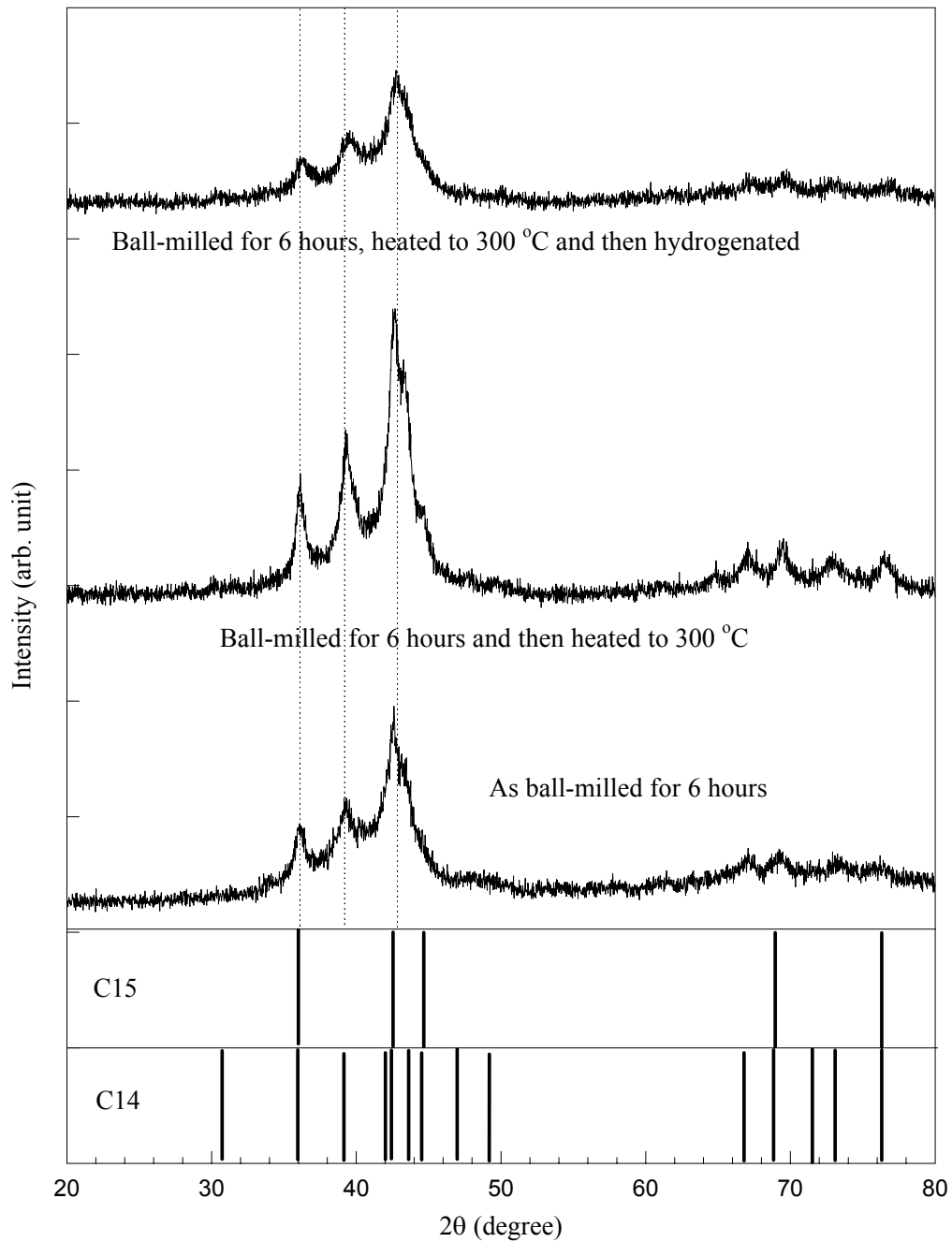
Figure 18. The XRD patterns of pure $Zr_{27}Ti_9Ni_{38}V_5Mn_{16}Cr_5$ ball-milled for 6 hours, ball-milled for 6 hours and then heated to 300 °C for 15 min, and ball-milled for 6 hours, heated to 300 °C, and then hydrogenated.

Figure 19 shows the results of the XRD measurements of LiAlH$_4$ + $Zr_{27}Ti_9Ni_{38}V_5Mn_{16}Cr_5$ taken in 1:1 volume ratio and ball-milled for 6 hours, ball-milled for 6 hours and then heated to 300 °C and held at this temperature for 15 min, and ball-milled for

6 hours, heated to 300 $^{\circ}$C, and then hydrogenated. After ball-milling for 6 hours, Bragg peaks of $Zr_{27}Ti_9Ni_{38}V_5Mn_{16}Cr_5$ broaden and shift to lower Bragg angles. Unlike in pure $Zr_{27}Ti_9Ni_{38}V_5Mn_{16}Cr_5$ ball-milled for 6 hours, this seems to be because all spherical particles are broken into pieces and not because the structures of $LiAlH_4$ + $Zr_{27}Ti_9Ni_{38}V_5Mn_{16}Cr_5$ taken in 1:1 volume ratio and ball-milled for 6 hours contain a larger fraction of an amorphous phase than those of $LiAlH_4$ + $Zr_{27}Ti_9Ni_{38}V_5Mn_{16}Cr_5$ taken in 1:1 volume ratio and ball-milled for 1 hour. This will be further discussed when comparing the results of hydrogenation behavior and also SEM micrograms. As discussed earlier, H_2, Al and LiH seem to be produced during ball-milling, though the peaks for Al and LiH are not clearly distinguishable this time because of the width of $Zr_{27}Ti_9Ni_{38}V_5Mn_{16}Cr_5$ peaks. After heating to 300 $^{\circ}$C, the peaks become sharper because of the stress relief and the relaxation of the structure, and shift back to the original peak positions. After hydrogenation, the peaks become broader and shift to lower Bragg angles even further when compared with the specimen as ball-milled for 6 hours, which indicates larger amount of absorbed hydrogen.
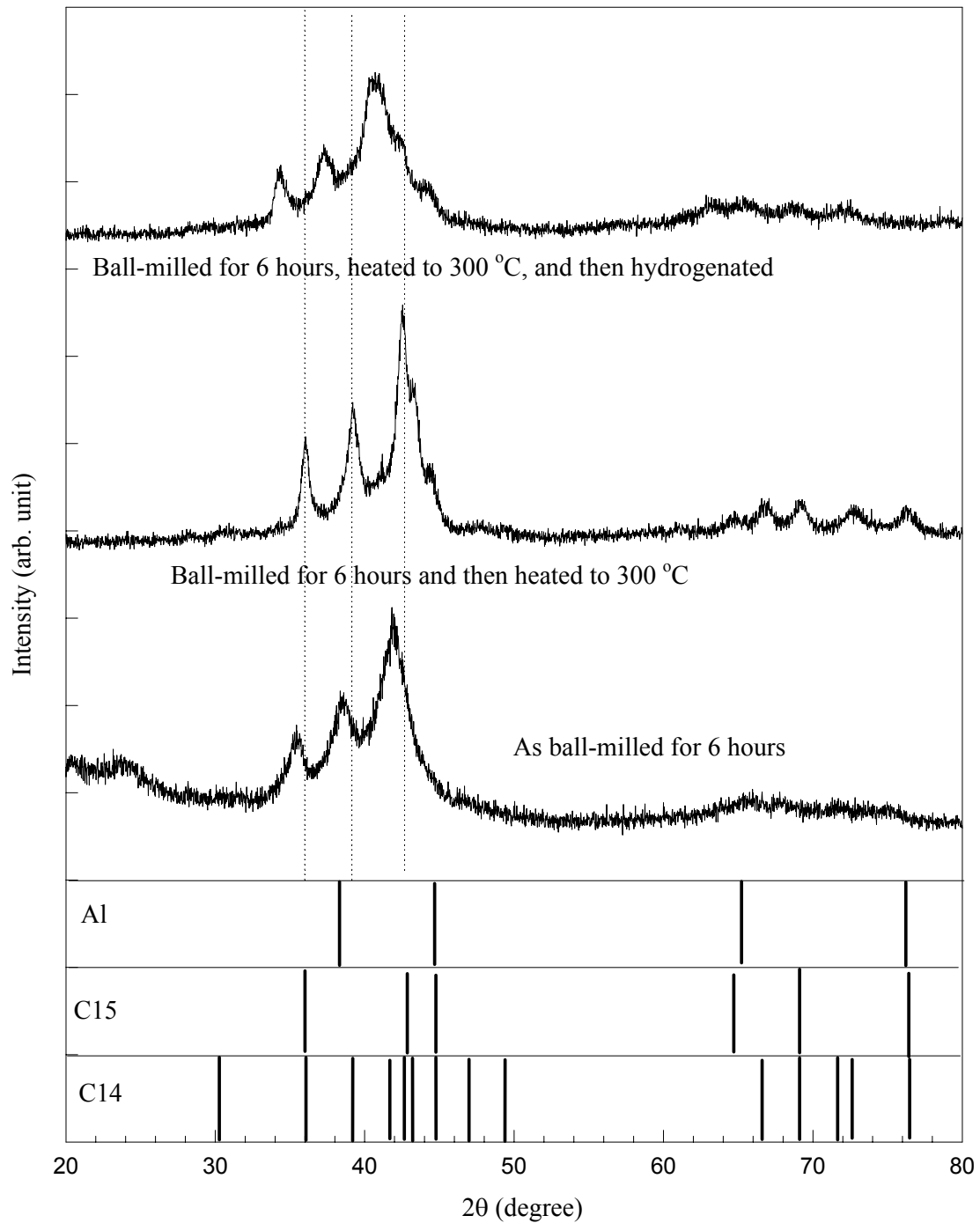
Figure 19. The XRD patterns of LiAlH$_4$ + Zr$_{27}$Ti$_9$Ni$_{38}$V$_5$Mn$_{16}$Cr$_5$ taken in 1:1 volume ratio and ball-milled for 6 hours, ball-milled for 6 hours and then heated to 300 ^{o}C for 15 min, and ball-milled for 6 hours, heated to 300 ^{o}C, and then hydrogenated.

Figure 20 shows the results of the DTA measurements of pure Zr$_{27}$Ti$_9$Ni$_{38}$V$_5$Mn$_{16}$Cr$_5$ ball-milled for 6 hours, ball-milled for 6 hours and then heated to 300

^{o}C and held at this temperature for 15 min, and ball-milled for 6 hours, heated to 300 ^{o}C, and then hydrogenated. No anomalies have been found after ball-milling for 6 hours, after heating to 300 ^{o}C, and after hydrogenation. This indicates that there is no crystallization events between 100 and 300 ^{o}C, and anomalies in DTA traces of $LiAlH_4$ + $Zr_{27}Ti_9Ni_{38}V_5Mn_{16}Cr_5$ ball-milled for 6 hours, if any, will not be due to the crystallization of amorphous phases, but will be intrinsic to the aluminohydride.
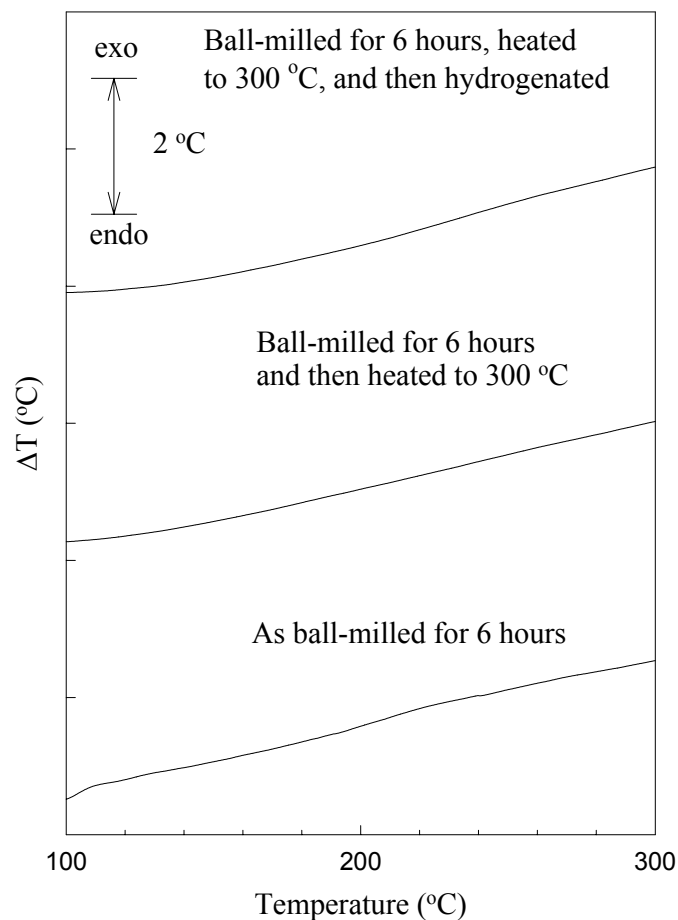
Figure 20. The DTA traces of pure $Zr_{27}Ti_9Ni_{38}V_5Mn_{16}Cr_5$ ball-milled for 6 hours, ball-milled for 6 hours and then heated to 300 ^{o}C for 15 min, and ball-milled for 6 hours, heated to 300 ^{o}C, and then hydrogenated.

Figure 21 shows the results of the DTA measurements of $LiAlH_4$ + $Zr_{27}Ti_9Ni_{38}V_5Mn_{16}Cr_5$ taken in 1:1 volume ratio and ball-milled for 6 hours, ball-milled for 6 hours and then heated to 300 ^{o}C and held at this temperature for 15 min, and ball-milled for

6 hours, heated to 300 ^{o}C, and then hydrogenated. After ball-milling for 6 hours, an endothermic peak which is similar to that of pure $Zr_{27}Ti_9Ni_{38}V_5Mn_{16}Cr_5$ ball-milled for 1 hour, heated to 300 ^{o}C, and then hydrogenated is found. Therefore this peak seems to be due to hydrogen evolution from $Zr_{27}Ti_9Ni_{38}V_5Mn_{16}Cr_5H_x$. No anomalies corresponding to the decomposition of $LiAlH_4$ or Li_3AlH_6 are found. This indicates that ball-milling for 6 hours induces the complete decomposition of both $LiAlH_4$ and Li_3AlH_6. No peak is found after heating to 300 ^{o}C for 15 min. After hydrogenation, the anomaly (100-200 ^{o}C) which is similar to that of pure $Zr_{27}Ti_9Ni_{38}V_5Mn_{16}Cr_5$ ball-milled for 1 hour, heated to 300 ^{o}C for 15 min, and then hydrogenated is found. Therefore this peak also seems to be due to hydrogen evolution from $Zr_{27}Ti_9Ni_{38}V_5Mn_{16}Cr_5H_x$, and $Zr_{27}Ti_9Ni_{38}V_5Mn_{16}Cr_5$ does not seem to work as a catalyst in the hydrogenation reaction to yield Li_3AlH_6 or $LiAlH_4$. The peak shifts to lower temperature by about 30 ^{o}C. This might be because of the lattice expansion due to much more absorbed hydrogen by the specimen after hydrogenation than by the one after ball-milling, which induces dehydrogenation at lower temperature.
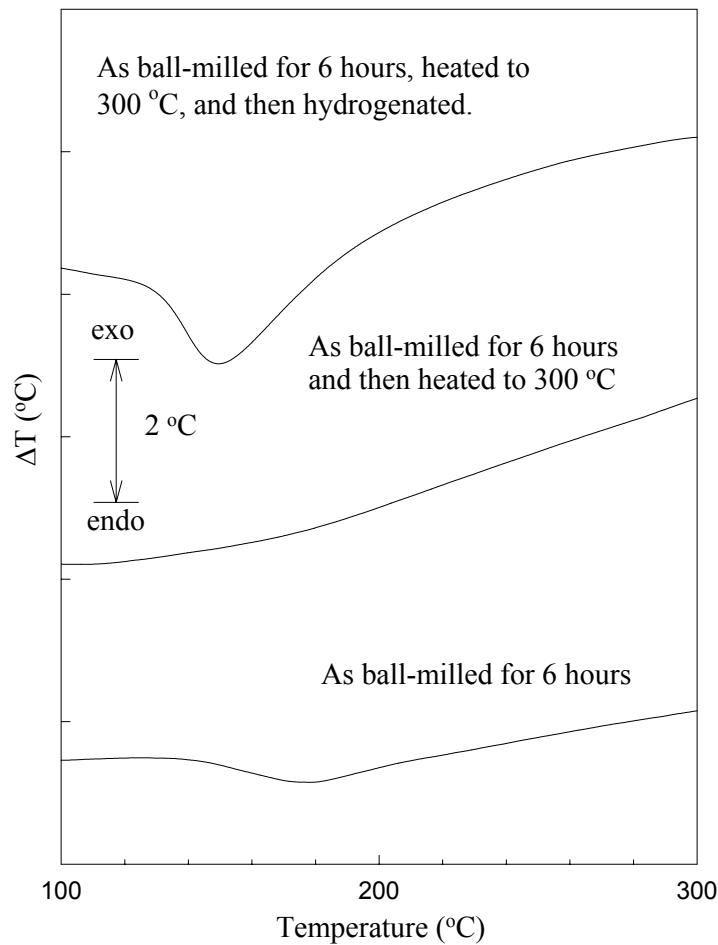
Figure 21. The DTA traces of $LiAlH_4 + Zr_{27}Ti_9Ni_{38}V_5Mn_{16}Cr_5$ taken in 1:1 volume ratio and ball-milled for 6 hours, ball-milled for 6 hours and then heated to 300 ^{o}C for 15 min, and ball-milled for 6 hours, heated to 300 ^{o}C, and then hydrogenated.

Figure 22 shows hydrogenation behavior of pure $Zr_{27}Ti_9Ni_{38}V_5Mn_{16}Cr_5$ ball-milled for 6 hours. The sample absorbed less than 0.2 wt% H_2. This low hydrogen absorption supports the assumption that the broadened Bragg peaks of pure $Zr_{27}Ti_9Ni_{38}V_5Mn_{16}Cr_5$ ball-milled for 6 hours are due to the presence of considerable amount of amorphous phases (See Figure 18).

Figure 23 shows hydrogenation behavior of $LiAlH_4 + Zr_{27}Ti_9Ni_{38}V_5Mn_{16}Cr_5$ taken in 1:1 volume ratio and ball-milled for 6 hours. The sample absorbed about 0.9 wt% H_2. Judging from the result of the DTA measurement and large shift of XRD pattern to lower Bragg angles as shown earlier, this seems to be due to hydrogen absorption by

$Zr_{27}Ti_9Ni_{38}V_5Mn_{16}Cr_5$. This high hydrogen absorption supports the suggestion that the broadened Bragg peaks of $LiAlH_4$ + $Zr_{27}Ti_9Ni_{38}V_5Mn_{16}Cr_5$ taken in 1:1 volume ratio and ball-milled for 6 hours are due to small particle sizes. The large difference of the amount of absorbed hydrogen by $LiAlH_4$ + $Zr_{27}Ti_9Ni_{38}V_5Mn_{16}Cr_5$ taken in 1:1 volume ratio and ball-milled for 6 hours and by $LiAlH_4$ + $Zr_{27}Ti_9Ni_{38}V_5Mn_{16}Cr_5$ taken in 1:1 volume ratio and ball-milled for 1 hour will be discussed when comparing SEM micrograms later.
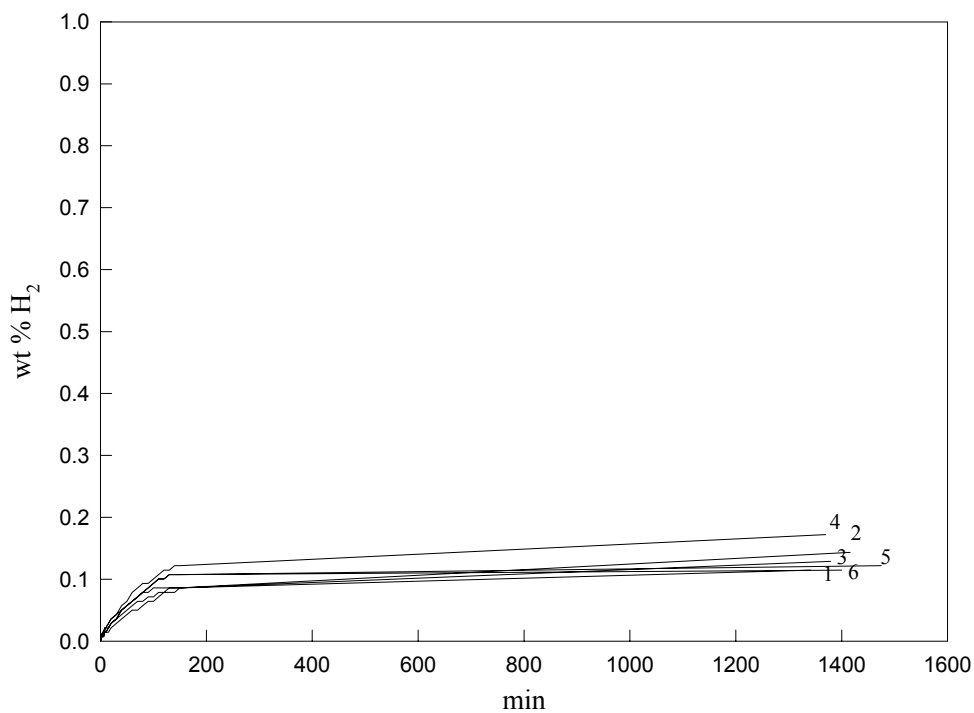
Figure 22. Hydrogenation behavior of pure $Zr_{27}Ti_9Ni_{38}V_5Mn_{16}Cr_5$ at 3.4-3.2 atm pressure at room temperature after ball-milling for 6 hours. The numeral next to the curve indicates hydrogenation cycle number.
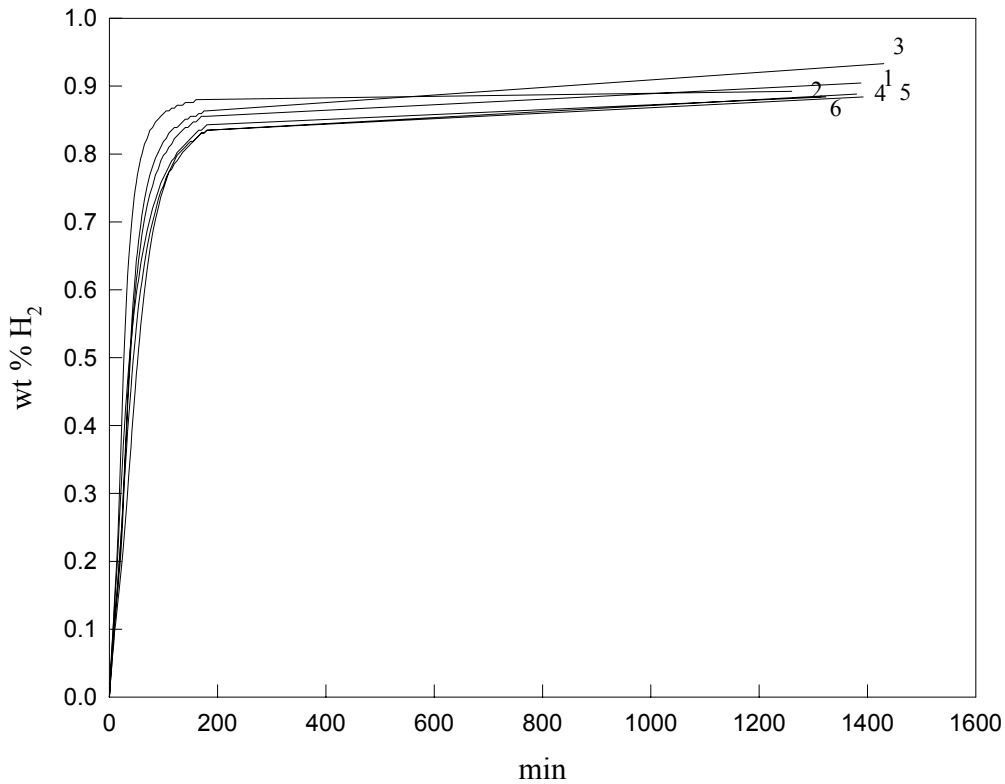
Figure 23. Hydrogenation behavior of LiAlH$_4$ + Zr$_{27}$Ti$_9$Ni$_{38}$V$_5$Mn$_{16}$Cr$_5$ at 3.3-1.8 atm pressure at room temperature taken in 1:1 volume ratio and ball-milled for 6 hours. The numeral next to the curve indicates hydrogenation cycle number.

Figure 24 shows the morphology of the particles of pure Zr$_{27}$Ti$_9$Ni$_{38}$V$_5$Mn$_{16}$Cr$_5$ ball-milled for 6 hours. The particles of Zr$_{27}$Ti$_9$Ni$_{38}$V$_5$Mn$_{16}$Cr$_5$ are heavily agglomerated thus it is difficult to establish individual particle sizes. However, the fraction of the particles smaller than 1 μm in pure Zr$_{27}$Ti$_9$Ni$_{38}$V$_5$Mn$_{16}$Cr$_5$ ball-milled for 6 hours seems to be nearly same as in pure Zr$_{27}$Ti$_9$Ni$_{38}$V$_5$Mn$_{16}$Cr$_5$ ball-milled for 1 hour. This indicates that the broadened Bragg peaks of pure Zr$_{27}$Ti$_9$Ni$_{38}$V$_5$Mn$_{16}$Cr$_5$ ball-milled for 6 hours are mainly due to its deeper amorphization (See Figure 18). This also explains lower hydrogen absorption of pure Zr$_{27}$Ti$_9$Ni$_{38}$V$_5$Mn$_{16}$Cr$_5$ ball-milled for 6 hours than that of pure Zr$_{27}$Ti$_9$Ni$_{38}$V$_5$Mn$_{16}$Cr$_5$ ball-milled for 1 hour (See Figure 13 and Figure 22).

Figure 25 shows the morphology of LiAlH$_4$ + Zr$_{27}$Ti$_9$Ni$_{38}$V$_5$Mn$_{16}$Cr$_5$ taken in 1:1 volume ratio and ball-milled for 6 hours. The sample particles are strongly agglomerated and

their average particle size is much smaller than that of $LiAlH_4 + Zr_{27}Ti_9Ni_{38}V_5Mn_{16}Cr_5$ taken in 1:1 volume ratio and ball-milled for 1 hour. This confirms that the broadened Bragg peaks of $LiAlH_4 + Zr_{27}Ti_9Ni_{38}V_5Mn_{16}Cr_5$ taken in 1:1 volume ratio and ball-milled for 6 hours are due to reduced particle sizes (See Figure 19). The spherical particles found in the specimen of $LiAlH_4 + Zr_{27}Ti_9Ni_{38}V_5Mn_{16}Cr_5$ taken in 1:1 volume ratio and ball-milled for 1 hour are no longer found in the specimen of $LiAlH_4 + Zr_{27}Ti_9Ni_{38}V_5Mn_{16}Cr_5$ taken in 1:1 volume ratio and ball-milled for 6 hours.

This explains that the specimen of $LiAlH_4 + Zr_{27}Ti_9Ni_{38}V_5Mn_{16}Cr_5$ taken in 1:1 volume ratio and ball-milled for 6 hours is well activated after the ball-milling, and thus it has much higher hydrogen capacity than that of the specimen of $LiAlH_4 + Zr_{27}Ti_9Ni_{38}V_5Mn_{16}Cr_5$ taken in 1:1 volume ratio and ball-milled for 1 hour (See Figure 14 and Figure 23).
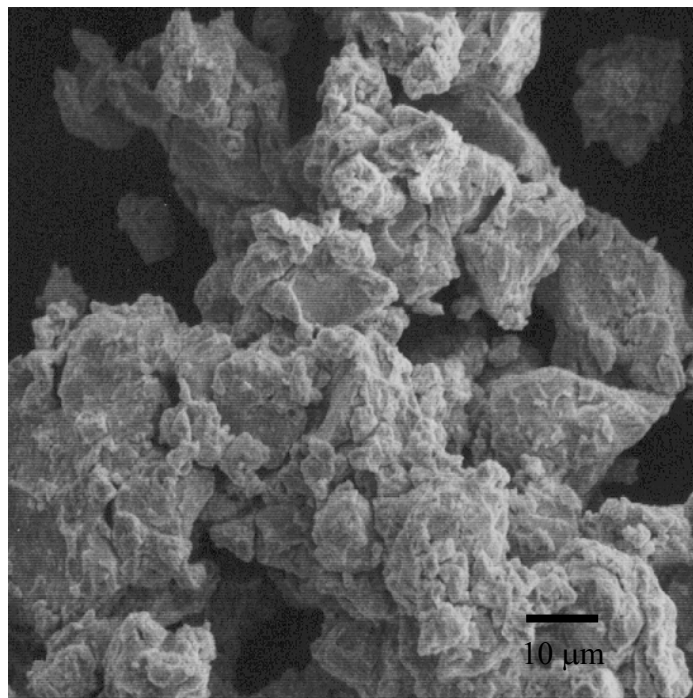
Figure 24. Morphology of pure $Zr_{27}Ti_9Ni_{38}V_5Mn_{16}Cr_5$ ball-milled for 6 hours (x 1000).
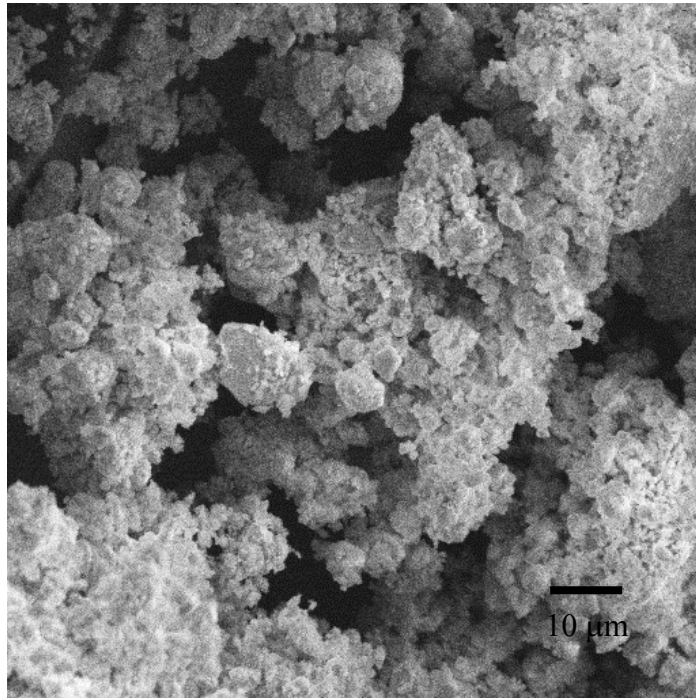
Figure 25. Morphology of LiAlH$_4$+Zr-Ti-Ni-V-Cr-Mn taken in 1:1 volume ratio and ball-milled for 6 hours (x 1000).

3.2 LiAlH$_4$ + LaNi$_{4.85}$Sn$_{0.15}$

3.2.1 After 1 Hour Ball-milling

Figure 26 shows the result of the XRD measurement of annealed LaNi$_{4.85}$Sn$_{0.15}$. The space group is P6/mmm and the lattice parameters were determined to be a=5.0601 (1) Å, c=4.0476 (1) Å.
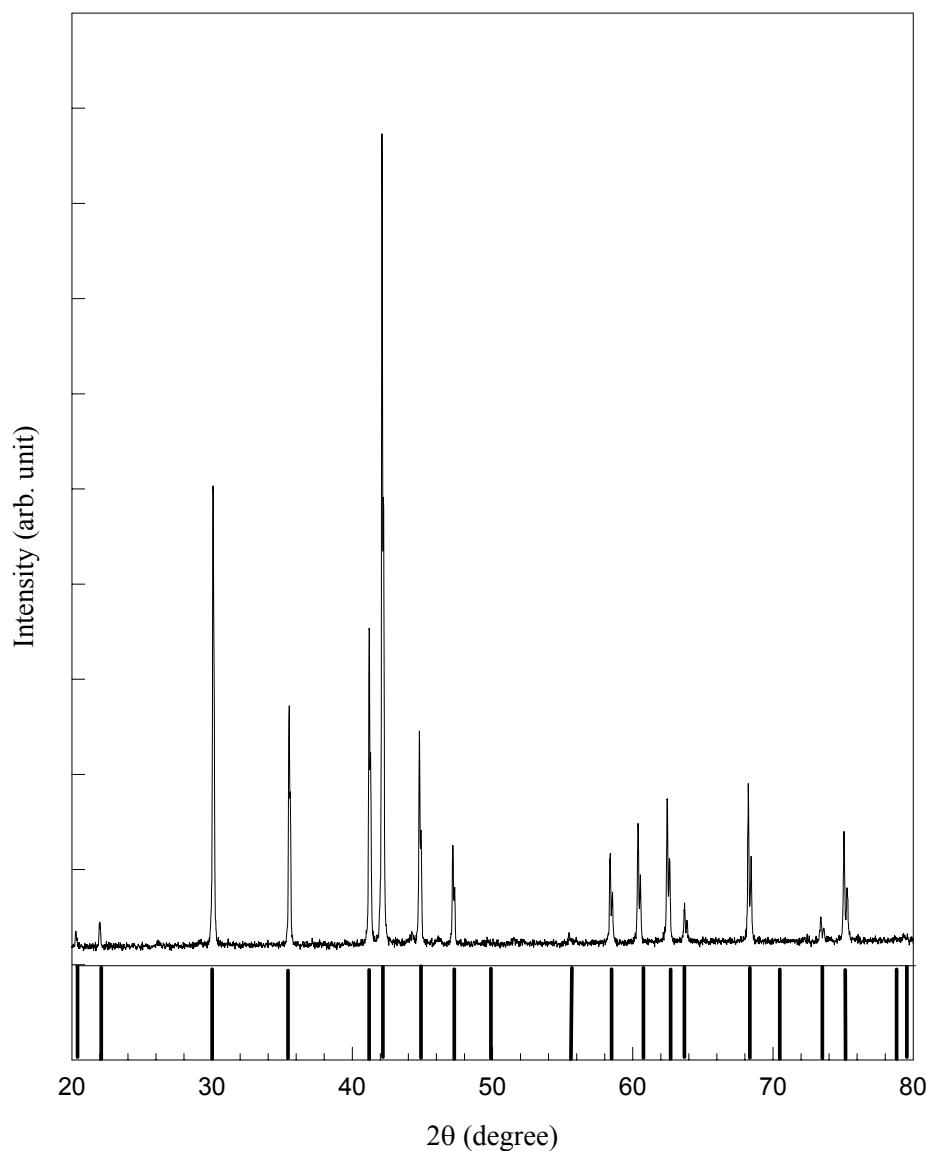

Figure 26. The XRD pattern of LaNi$_{4.85}$Sn$_{0.15}$ annealed at 950 $^{\circ}$C for 6 hours.

Figure 27 shows the results of the XRD measurements of pure LaNi$_{4.85}$Sn$_{0.15}$ ball-milled for 1 hour, ball-milled for 1 hour and then heated to 300 $^{\circ}$C and held at this

temperature for 15 min, and ball-milled for 1 hour, heated to 300 $^{\circ}$C, and then hydrogenated. After ball-milling for 1 hour, the Bragg peaks of LaNi$_{4.85}$Sn$_{0.15}$ broaden, which indicates its partial amorphization and reduced particle size. After heating to 300 $^{\circ}$C, the peaks of LaNi$_{4.85}$Sn$_{0.15}$ become sharper because of the stress relief and the relaxation of the structure. The peaks of Ni are found but they are not very distinct. After hydrogenation, the peaks of LaNi$_{4.85}$Sn$_{0.15}$ become broader again, and the peaks of Ni and LaH$_2$ are found.
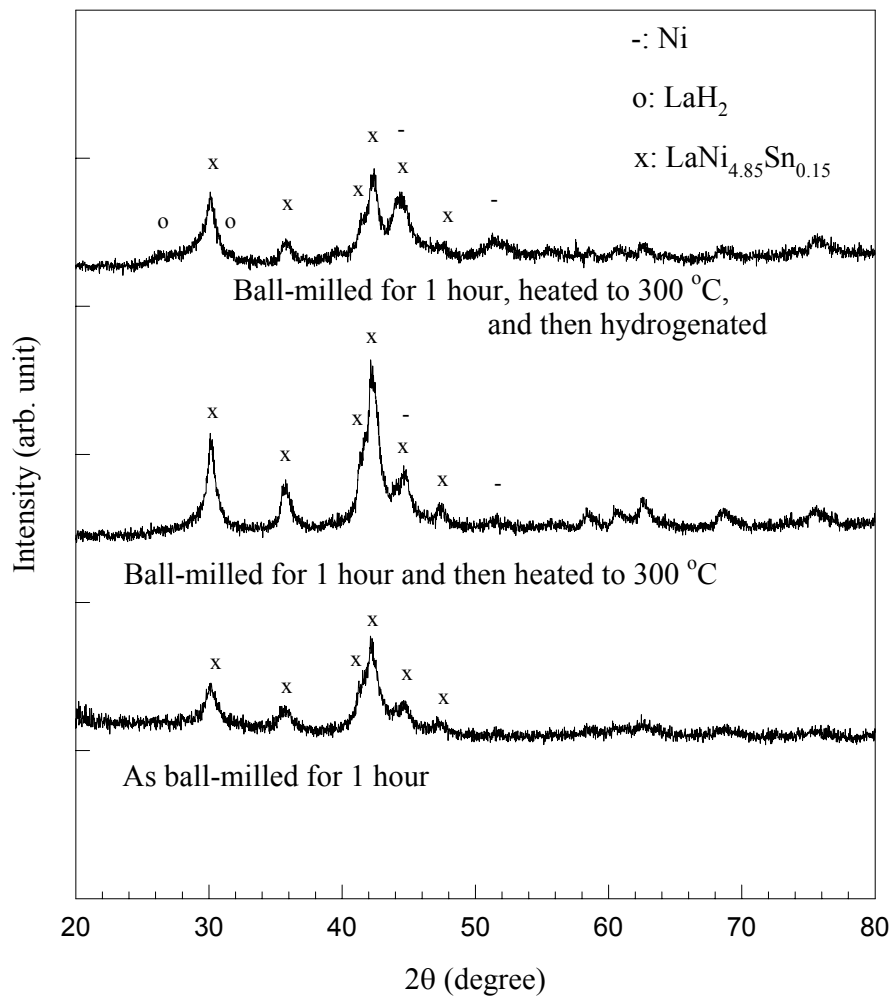
Figure 27. The XRD patterns of pure LaNi$_{4.85}$Sn$_{0.15}$ ball-milled for 1 hour, ball-milled for 1 hour and then heated to 300 $^{\circ}$C for 15 min, and ball-milled for 1 hour, heated to 300 $^{\circ}$C, and then hydrogenated.

Figure 28 shows the results of the XRD measurements of $LiAlH_4 + LaNi_{4.85}Sn_{0.15}$ taken in 1:1 volume ratio and ball-milled for 1 hour, ball-milled for 1 hour and then heated to 300 °C and held at this temperature for 15 min, and ball-milled for 1 hour, heated to 300 °C, and then hydrogenated. After ball-milling for 1 hour, no peaks of $LiAlH_4$ or Li_3AlH_6 are found. Instead, the peaks of Al and/or LiH are found. This means that hydrogen evolves during ball-milling because of the decomposition of $LiAlH_4$. However, the peaks of $LaNi_{4.85}Sn_{0.15}$ do not shift to lower Bragg angles, and no peaks of $LaNi_{4.85}Sn_{0.15}H_x$ are found. This means that hydrogen evolved during decomposition of $LiAlH_4$ is not dissolved in $LaNi_{4.85}Sn_{0.15}$, as it is the case when $Zr_{27}Ti_9Ni_{38}V_5Mn_{16}Cr_5$ is ball-milled with $LiAlH_4$. The peaks of $LaNi_{4.85}Sn_{0.15}$ are not broad, but rather sharp. This indicates that $LiAlH_4$ works as a shock absorber as it does in $Zr_{27}Ti_9Ni_{38}V_5Mn_{16}Cr_5$, and that the specimen of $LaNi_{4.85}Sn_{0.15}$ is not amorphized so much.

After heating to 300 °C, the peaks corresponding to LaH_2 are found. This is because the reaction shown in equation (3.1) is thermodynamically favorable when compared with the hydrogenation reaction shown in equation (3.2).

$$LaNi_5 + H_2 = LaH_2 + 5Ni, \quad \Delta G = -80.2 + 0.148T \quad (kcal/mol\ H_2) \quad (3.1)$$

$$1/3LaNi_5 + H_2 = 1/3LaNi_5H_6, \quad \Delta G = -30.9 + 0.109T \ (kcal/mol\ H_2) \quad (3.2)$$
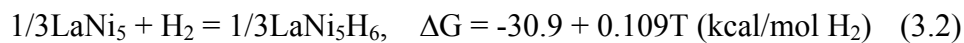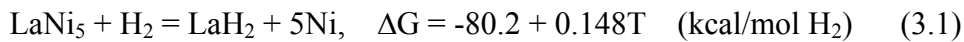
However, at room temperature the reaction shown in equation (3.2) is usually observed because it is kinetically favorable [23]. The peaks of Ni are not found because Ni phase seem to be amorphous and because the amount of Ni is small. As shown in the result of DTA measurements later, Li_3AlH_6 is not decomposed by 1 hour ball-milling. Hydrogen evolved from Li_3AlH_6 during heating to 300 °C seems to react with $LaNi_{4.85}Sn_{0.15}$ and produce LaH_2 and Ni phases.

After hydrogenation, the Bragg peaks of $LaNi_{4.85}Sn_{0.15}$ become smaller, and the peaks of $LaNi_{4.85}Sn_{0.15}H_x$ (x ~ 3.8) are found. The peaks corresponding to LaH_2 remain the

same.
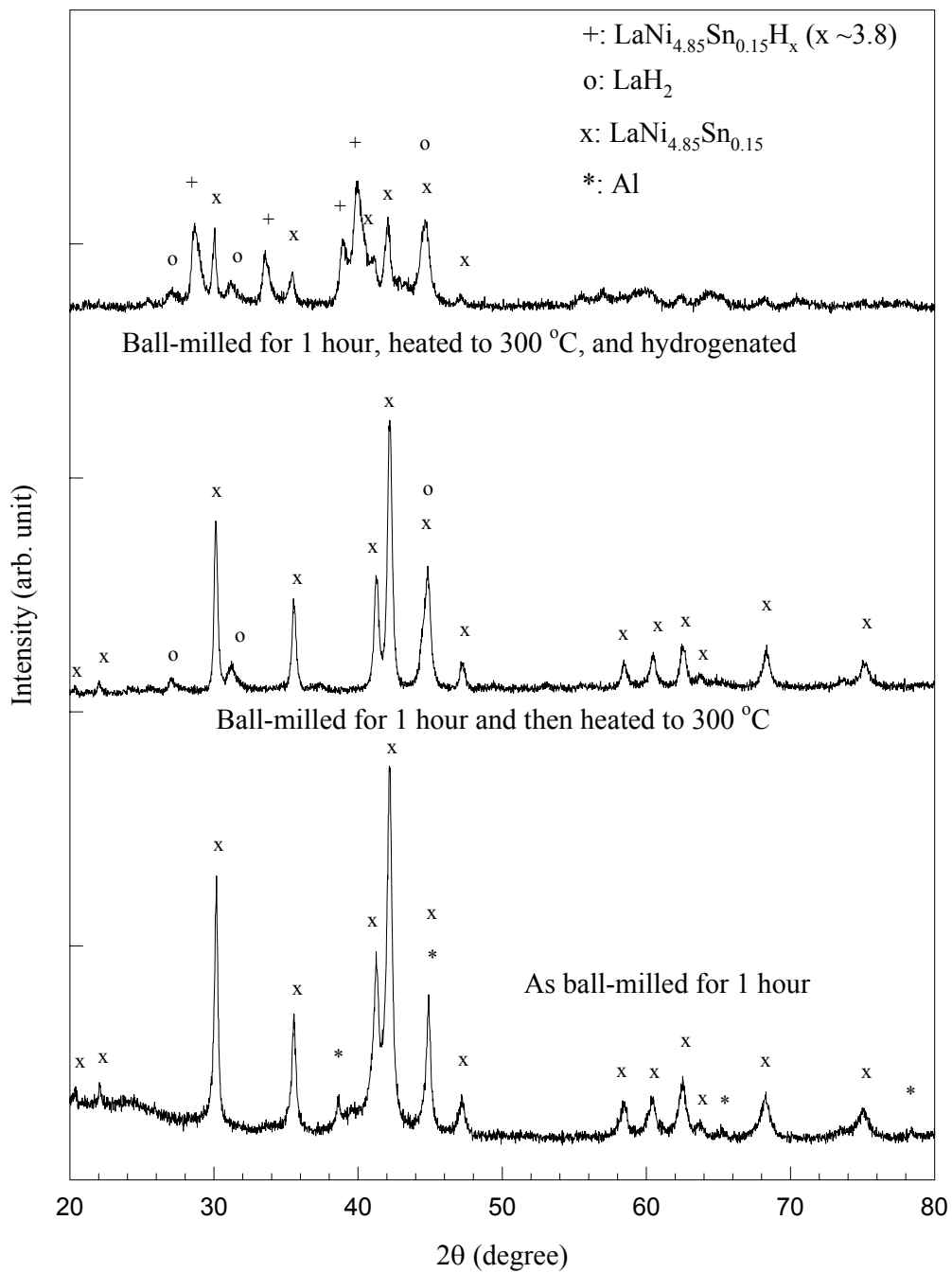

Figure 28. The XRD patterns of LiAlH$_4$ + LaNi$_{4.85}$Sn$_{0.15}$ taken in 1:1 volume ratio and ball-milled for 1 hour, ball-milled for 1 hour and then heated to 300 ^{o}C for 15 min, and ball-milled for 1 hour, heated to 300 ^{o}C, and then hydrogenated.

Figure 29 shows the results of the DTA measurements of pure $LaNi_{4.85}Sn_{0.15}$ ball-milled for 1 hour, ball-milled for 1 hour and then heated to 300 ^{o}C and held at this temperature for 15 min, and ball-milled for 1 hour, heated to 300 ^{o}C, and then hydrogenated. No anomalies are found after ball-milling for 1 hour, after heating up to 300 ^{o}C, and after hydrogenation. This indicates that there is no crystallization in the ball-milled $LaNi_{4.85}Sn_{0.15}$ between 100 and 300 ^{o}C.
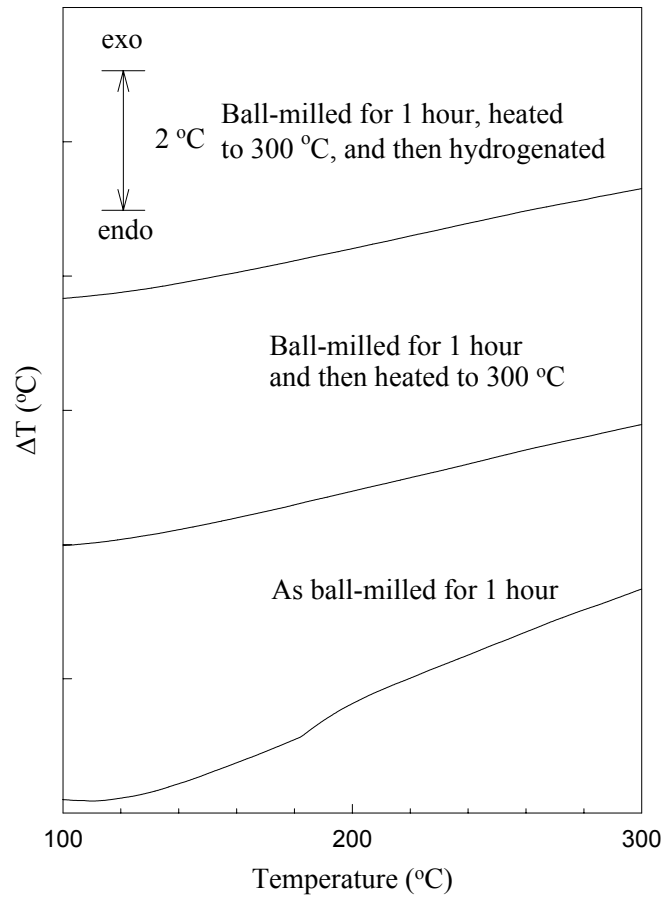
Figure 29. The DTA traces of pure $LaNi_{4.85}Sn_{0.15}$ ball-milled for 1 hour, ball-milled for 1 hour and then heated to 300 ^{o}C for 15 min, and ball-milled for 1 hour, heated to 300 ^{o}C, and then hydrogenated.

Figure 30 shows the results of the DTA measurements of $LiAlH_4$ + $LaNi_{4.85}Sn_{0.15}$ ball-milled for 1 hour, ball-milled for 1 hour and then heated to 300 ^{o}C and held at this

temperature for 15 min, and ball-milled for 1 hour, heated to 300 $^{\circ}$C, and then hydrogenated. After ball-milling for 1 hour, a broad peak which is similar to that observed during the decomposition of Li_3AlH_6 is found. This indicates that ball-milling for 1 hour induces the decomposition of $LiAlH_4$ into Li_3AlH_6, Al, and H_2. The peak shifts to lower temperature when compared to the corresponding peak of pure Li_3AlH_6. No anomalies are found after heating to 300 $^{\circ}$C. After hydrogenation, a broad peak is found (100-170 $^{\circ}$C). This seems to be due to de-hydrogenation of $LaNi_{4.85}Sn_{0.15}H_x$ (x ~ 3.8).
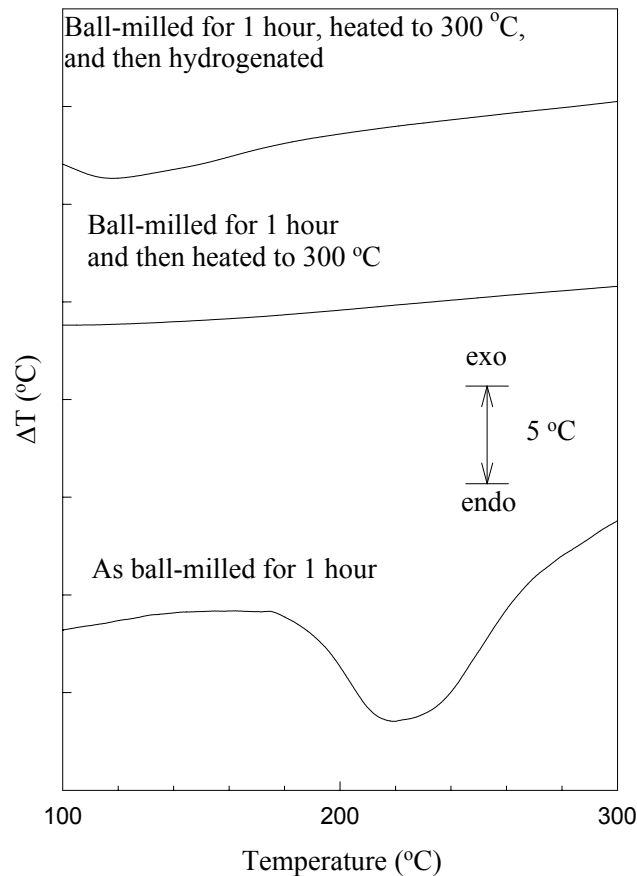
Figure 30. The DTA traces of $LiAlH_4$ + $LaNi_{4.85}Sn_{0.15}$ taken in 1:1 volume ratio and ball-milled for 1 hour, ball-milled for 1 hour and then heated to 300 $^{\circ}$C for 15 min, and ball-milled for 1 hour, heated to 300 $^{\circ}$C, and then hydrogenated.

Figure 31 shows hydrogenation behavior of pure $LaNi_{4.85}Sn_{0.15}$ ball-milled for 1 hour. The sample absorbed about 0.2 wt% H_2. This low hydrogen capacity seems to be due

to its amorphous phases which are confirmed by the XRD measurement earlier (See Figure 27).

Figure 32 shows hydrogenation behavior of $LiAlH_4$ + $LaNi_{4.85}Sn_{0.15}$ taken in 1:1 volume ratio and ball-milled for 1 hour. After 2 cycles, the sample is activated, and it absorbs about 0.6 wt% H_2. More than 80 % of hydrogen capacity is absorbed within 20 minutes. The higher hydrogen capacity of this specimen when compared to that of pure $LaNi_{4.85}Sn_{0.15}$ is observed due to a better crystallinity, which is confirmed by the XRD measurement earlier (See Figure 28).
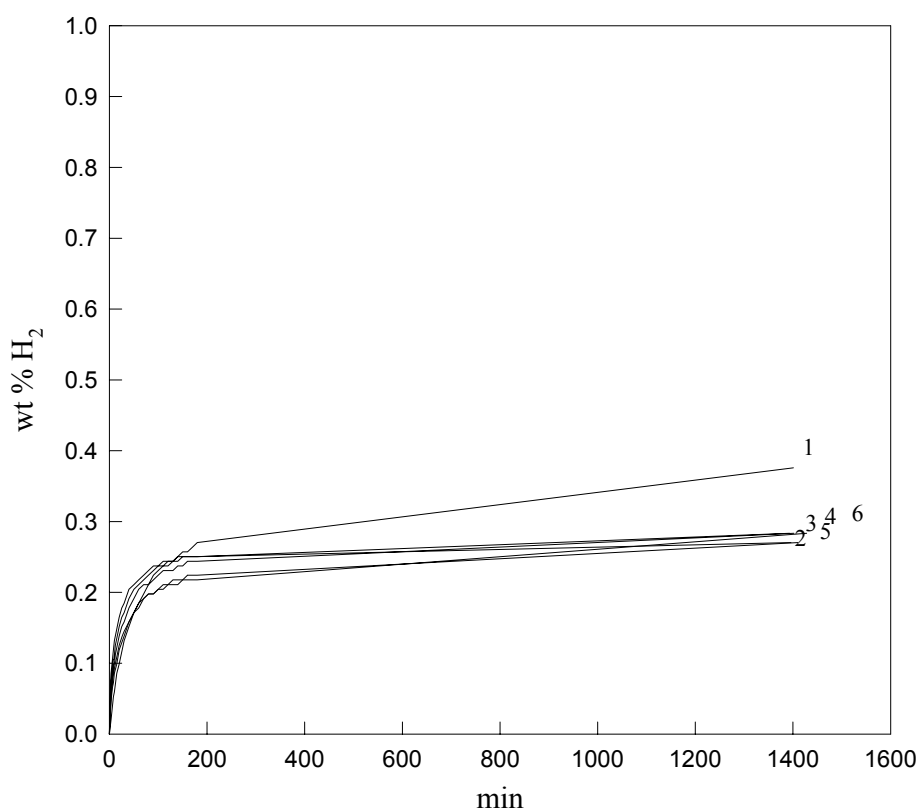
Figure 31. Hydrogenation behavior of pure $LaNi_{4.85}Sn_{0.15}$ at 3.4-3.1 atm pressure at room temperature after ball-milling for 1 hour. The numeral next to the curve indicates hydrogenation cycle number.
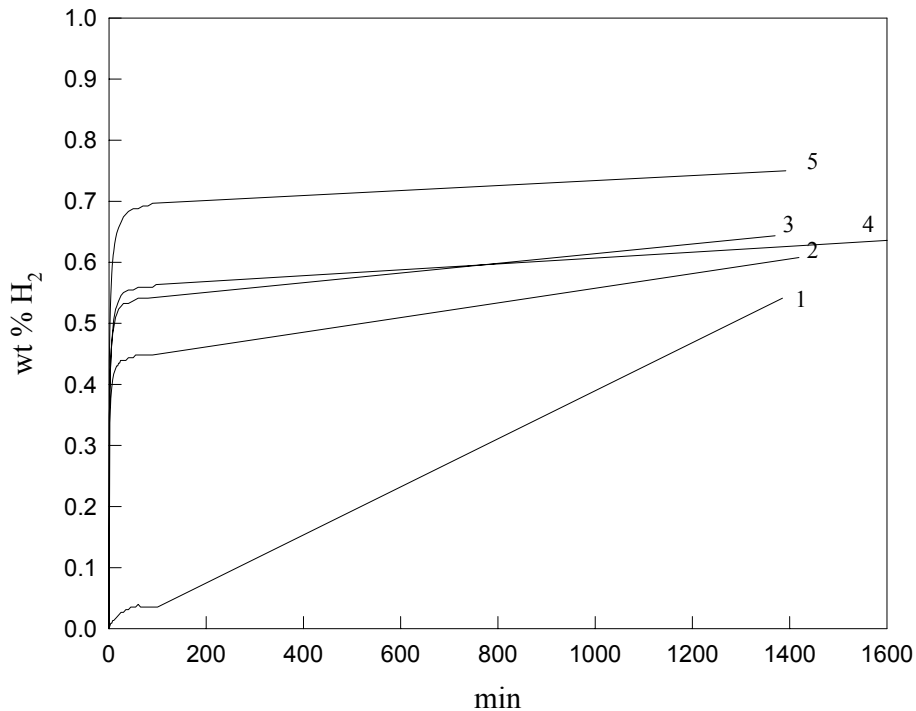
Figure 32. Hydrogenation behavior of $LiAlH_4$ + $LaNi_{4.85}Sn_{0.15}$ at 3.3-2.2 atm pressure at room temperature taken in 1:1 volume ratio and ball-milled for 1 hour. The numeral next to the curve indicates hydrogenation cycle number.

Figure 33 shows the morphology of the particles of as gas atomized $LaNi_{4.85}Sn_{0.15}$. The shapes are spherical and the sizes of the particles are distributed from 2 to 50 μm.

Figure 34 shows the morphology of the particles of $LaNi_{4.85}Sn_{0.15}$ ball-milled for 1 hour. No spherical particles are present and the particles are strongly agglomerated. The sizes of the particles vary from less than 1 to 35 μm.

Figure 35 shows the morphology of the particles of $LiAlH_4$ + $LaNi_{4.85}Sn_{0.15}$ taken in 1:1 volume ratio as ball-milled for 1 hour. The sizes of the sample particles are distributed from less than 1 to 15 μm. The average particle size of $LaNi_{4.85}Sn_{0.15}$ in this specimen is much smaller than that of pure $LaNi_{4.85}Sn_{0.15}$ ball-milled for 1 hour. Since the smaller particles have larger surface area in total, this explains quick hydrogen absorption property of $LiAlH_4$ + $LaNi_{4.85}Sn_{0.15}$ taken in 1:1 volume ratio and ball-milled for 1 hour.

48

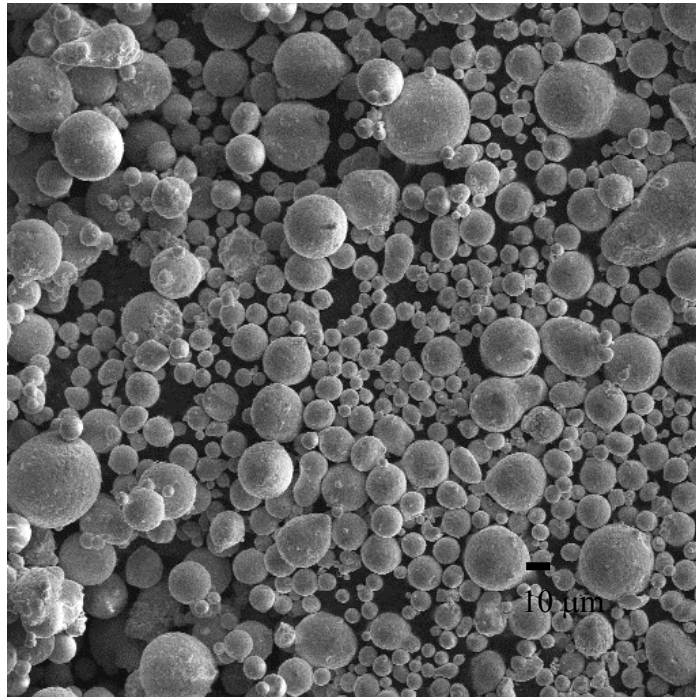Figure 33. Morphology of annealed LaNi$_{4.85}$Sn$_{0.15}$ (x 300).

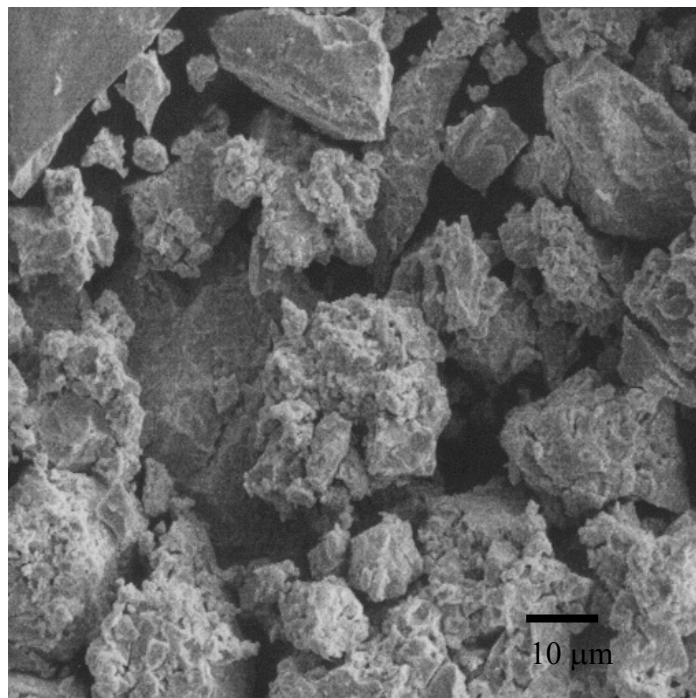Figure 34. Morphology of pure LaNi$_{4.85}$Sn$_{0.15}$ ball-milled for 1 hour (x 1000).
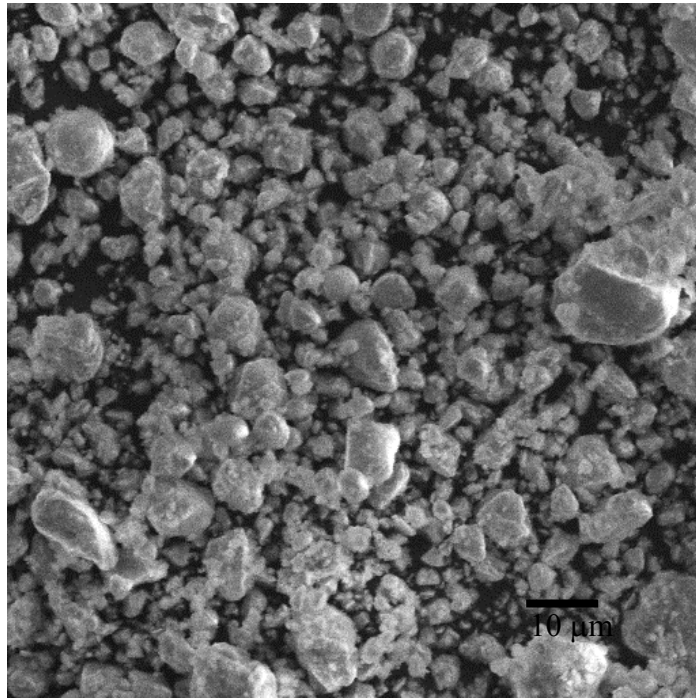
Figure 35. Morphology of LiAlH$_4$ + LaNi$_{4.85}$Sn$_{0.15}$ taken in 1:1 volume ratio and ball-milled for 1 hour (x 1000).

3.2.2 After 6 Hour Ball-milling

Figure 36 shows the results of the XRD measurements of pure $LaNi_{4.85}Sn_{0.15}$ ball-milled for 6 hours, ball-milled for 6 hours and then heated to 300 ^{o}C and held at this temperature for 15 min, and ball-milled for 6 hours, heated to 300 ^{o}C, and then hydrogenated. After ball-milling for 6 hours, the Bragg peaks corresponding to $LaNi_{4.85}Sn_{0.15}$ become broader than those of pure $LaNi_{4.85}Sn_{0.15}$ ball-milled for 1 hour. This is due to further amorphization of pure $LaNi_{4.85}Sn_{0.15}$ ball-milled for 6 hours, which will be discussed later with the hydrogenation behavior of pure $LaNi_{4.85}Sn_{0.15}$ ball-milled for 6 hours. After heating to 300 ^{o}C and after hydrogenation, no significant change is observed.

Figure 37 shows the results of the XRD measurements of $LiAlH_4$ + $LaNi_{4.85}Sn_{0.15}$ taken in 1:1 volume ratio and ball-milled for 6 hours, ball-milled for 6 hours and then heated to 300 ^{o}C and held at this temperature for 15 min, and ball-milled for 6 hours, heated to 300 ^{o}C, and then hydrogenated. After ball-milling for 6 hours, the broadened peaks corresponding to LaH_2 and Ni are found. The reaction shown in equation (3.1) does not occur at room temperature because atoms are not highly mobile. However, it can occur when the kinetic constraints are relieved by ball-milling. After heating to 300 ^{o}C, the peaks of LaH_2 disappear, and the peaks of $LaNi_{4.85}Sn_{0.15}$ and unknown phases appear. This is unexpected because LaH_2 is so stable that it does not decompose below 300 ^{o}C, and also because LaH_2 is thermodynamically more stable than $LaNi_{4.85}Sn_{0.15}$. The cause remains unknown. After hydrogenation, the sharp peaks of LaH_2 and Ni are found. This cause also remains unknown.
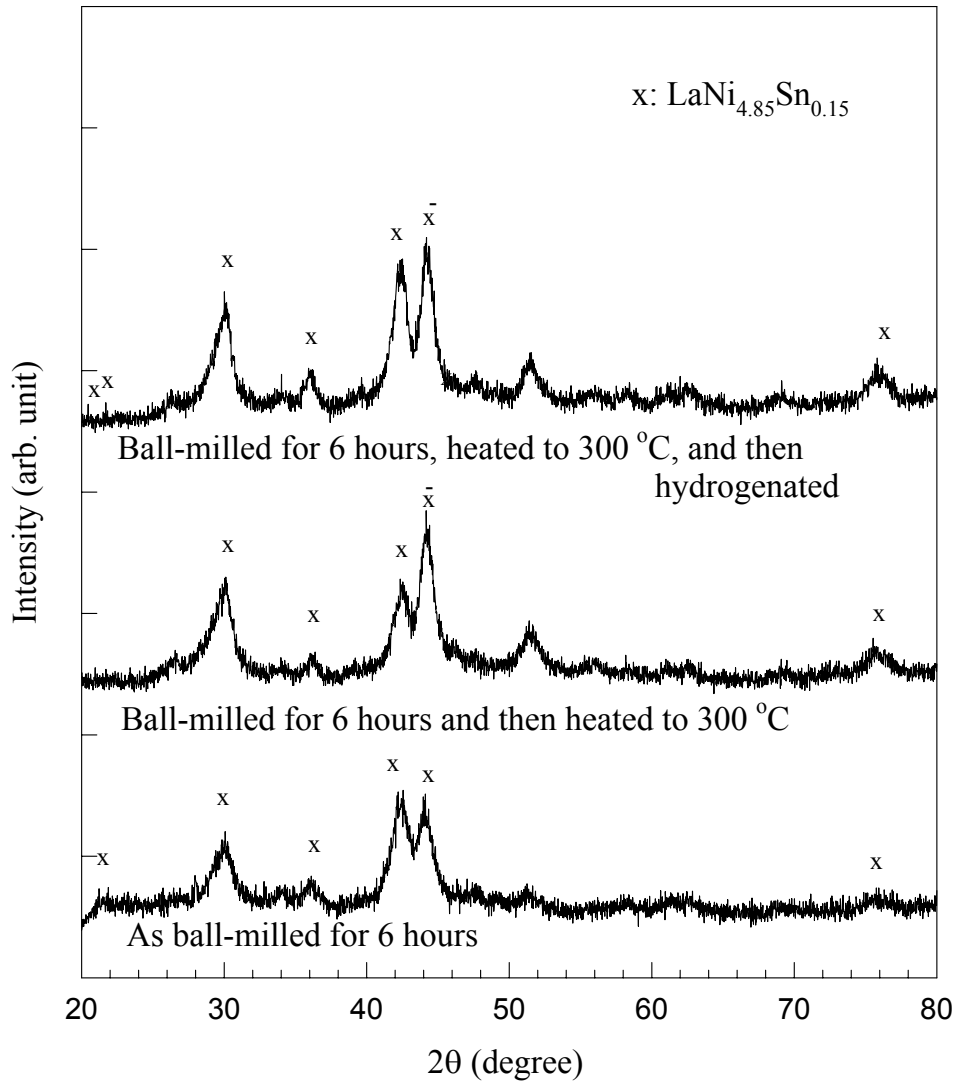
Figure 36. The XRD patterns of pure LaNi$_{4.85}$Sn$_{0.15}$ ball-milled for 6 hours, ball-milled for 6 hours and then heated to 300 $^{\circ}$C for 15 min, and ball-milled for 6 hours, heated to 300 $^{\circ}$C, and then hydrogenated.
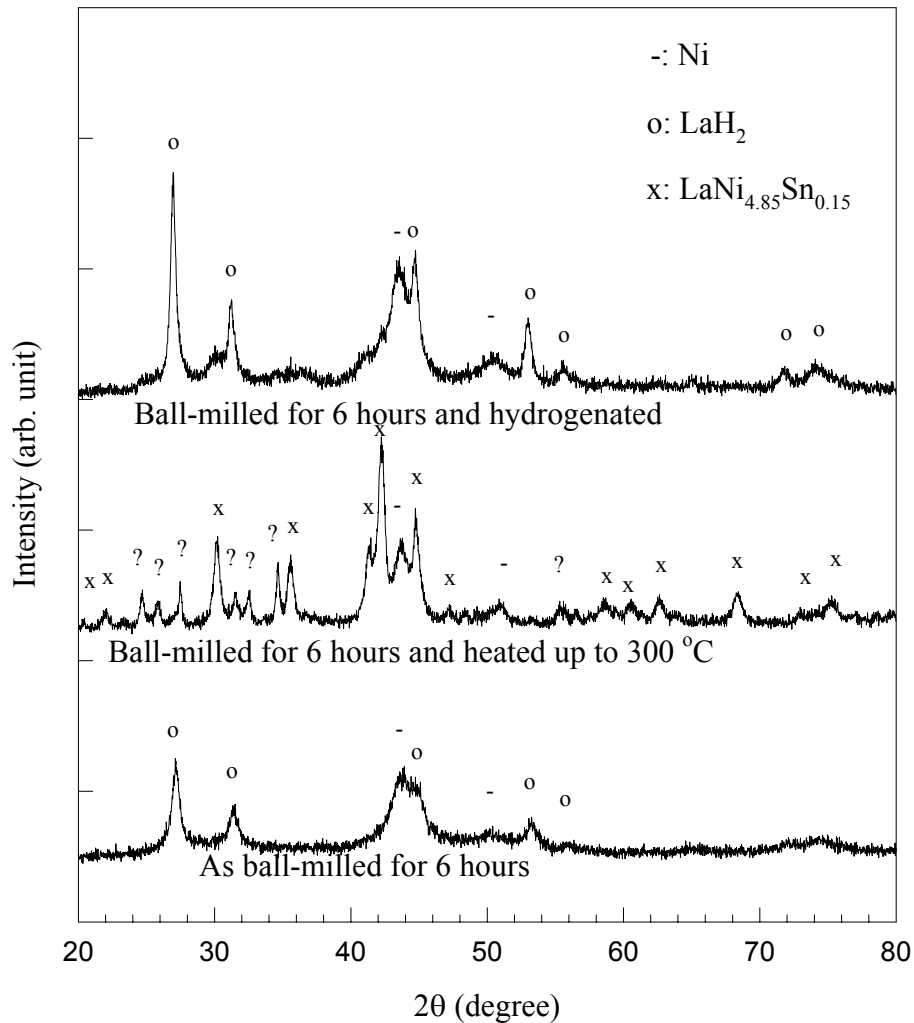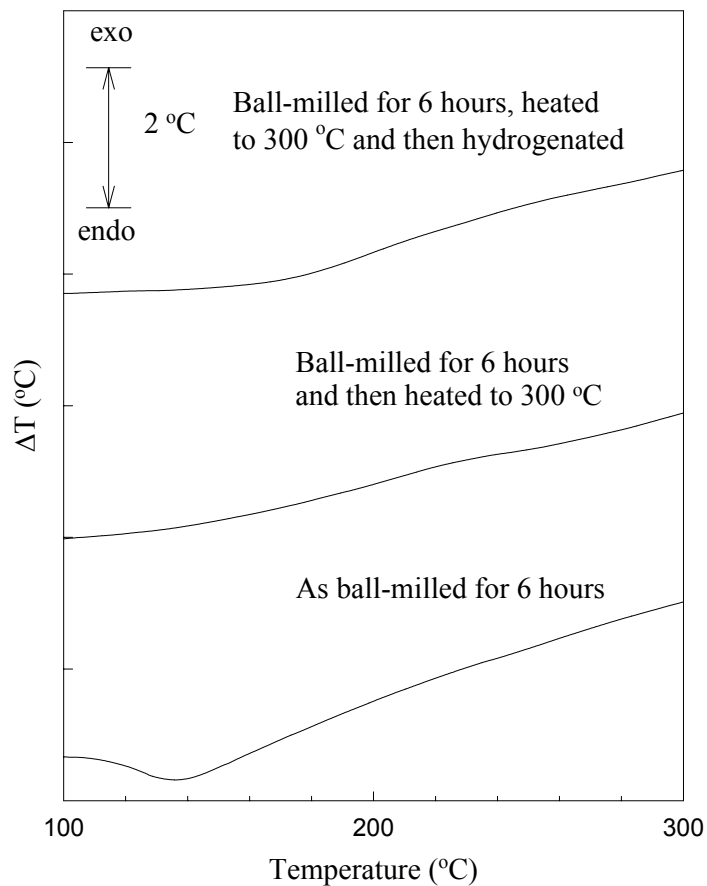
Figure 37. The XRD patterns of LiAlH$_4$ + LaNi$_{4.85}$Sn$_{0.15}$ taken in 1:1 volume ratio and ball-milled for 6 hours, ball-milled for 6 hours and then heated to 300 ^{o}C for 15 min, and ball-milled for 6 hours, heated to 300 ^{o}C, and then hydrogenated.

The DTA measurements of pure LaNi$_{4.85}$Sn$_{0.15}$ ball-milled for 6 hours were not done, because the phases of LiAlH$_4$ + LaNi$_{4.85}$Sn$_{0.15}$ taken in 1:1 volume ratio and ball-milled for 6 hours are different from those of pure LaNi$_{4.85}$Sn$_{0.15}$ ball-milled for 6 hours.

Figure 38 shows the results of the DTA measurements of LiAlH$_4$ + LaNi$_{4.85}$Sn$_{0.15}$ ball-milled for 6 hours, ball-milled for 6 hours and then heated to 300 ^{o}C and held at this temperature for 15 min, and ball-milled for 6 hours, heated to 300 ^{o}C, and then hydrogenated. After ball-milling for 6 hours, one broad peak seemingly corresponding to the formation of the

unknown phase(s) is found. No anomalies are found after heating to 300 ^{o}C. This confirms that the unknown phases are thermodynamically stable. However, after hydrogenation, no anomalies are found either. Since the phases in the specimen ball-milled for 6 hours are the same as those in the one ball-milled for 6 hours, heated to 300 ^{o}C, and then hydrogenated, the same peak should be found. This may be because after 6 hours ball-milling the LaH$_2$ phase is amorphous (See Figure 37), and thus it becomes thermodynamically unstable.

Figure 38. The DTA traces of LiAlH$_4$ + LaNi$_{4.85}$Sn$_{0.15}$ taken in 1:1 volume ratio and ball-milled for 6 hours, ball-milled for 6 hours and then heated to 300 ^{o}C for 15 min, and ball-milled for 6 hours, heated to 300 ^{o}C, and then hydrogenated.

Figure 39 shows hydrogenation behavior of pure LaNi$_{4.85}$Sn$_{0.15}$ ball-milled for 6 hours. The sample absorbs less than 0.2 wt% H$_2$. The lower hydrogen capacity of pure LaNi$_{4.85}$Sn$_{0.15}$

ball-milled for 6 hours than that of pure $LaNi_{4.85}Sn_{0.15}$ ball-milled for 1 hour could be attributed to the larger amount of amorphous phases after longer processing.

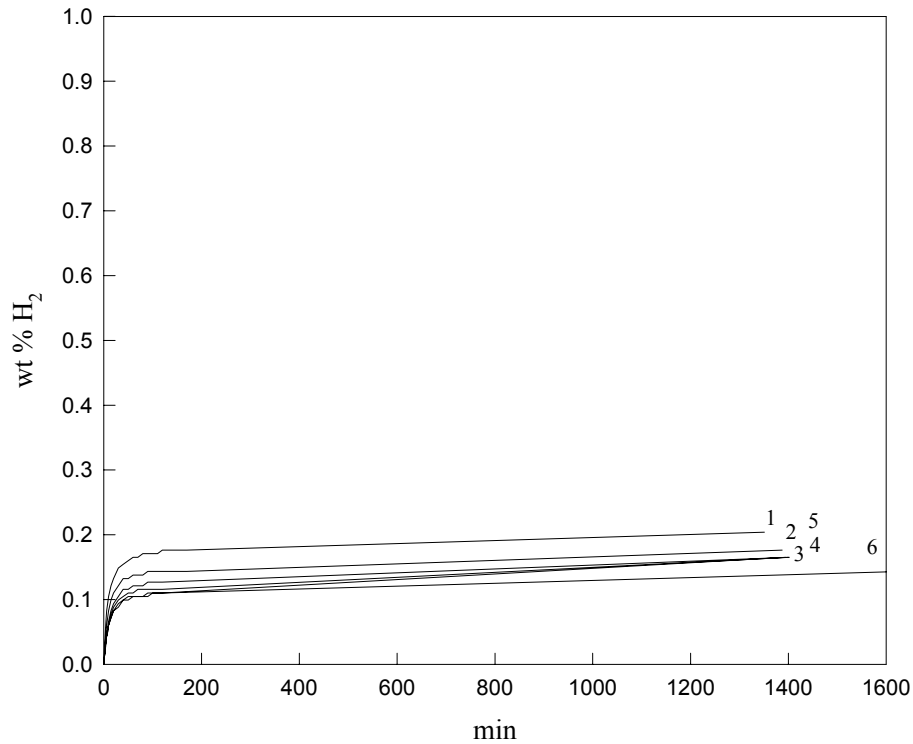Figure 39. Hydrogenation behavior of pure $LaNi_{4.85}Sn_{0.15}$ at 3.4-3.1 atm pressure at room temperature after ball-milling for 6 hours. The numeral next to the curve indicates hydrogenation cycle number.

Figure 40 shows hydrogenation traces of $LiAlH_4$ + $LaNi_{4.85}Sn_{0.15}$ taken in 1:1 volume ratio and ball-milled for 6 hours. The sample absorbs about 0.2 wt% H_2 slowly. This is because the LaH_2 phases are dominant and only a small portion of $LaNi_5$-based phases exists as revealed by the XRD measurement earlier (See Figure 37).
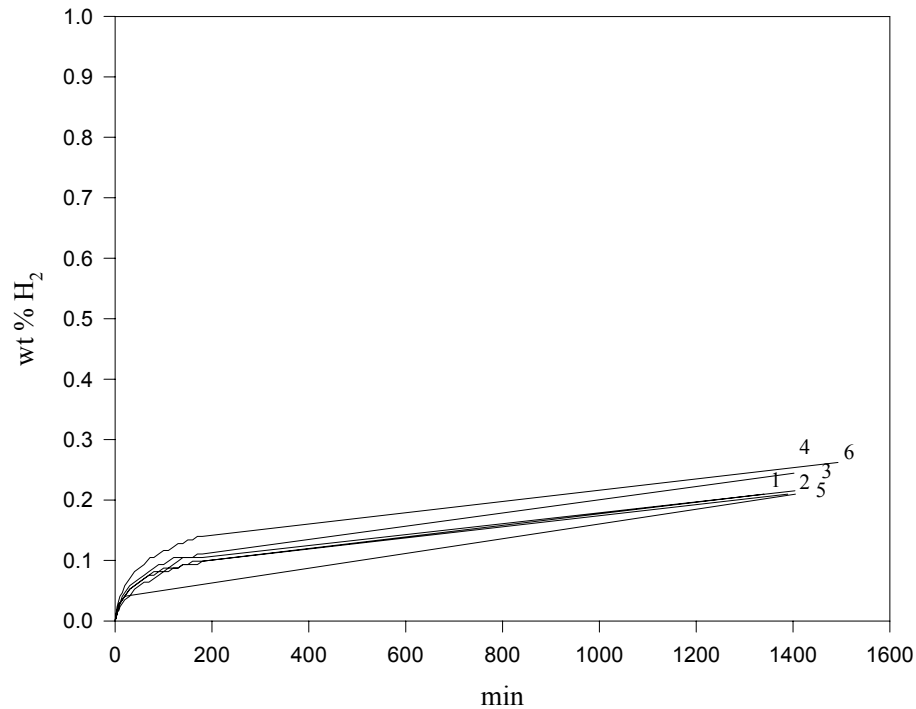
Figure 40. Hydrogenation behavior of LiAlH$_4$ + LaNi$_{4.85}$Sn$_{0.15}$ at 3.4-3.1 atm pressure at room temperature taken in 1:1 volume ratio and ball-milled for 6 hours. The numeral next to the curve indicates hydrogenation cycle number.

Figure 41 shows the morphology of the particles of pure LaNi$_{4.85}$Sn$_{0.15}$ ball-milled for 6 hours. The sizes of the particles vary from less than 1 to 30 μm. The number of large particles, which are larger than 25 μm, in pure LaNi$_{4.85}$Sn$_{0.15}$ ball-milled for 6 hours decreases when compared with that of pure LaNi$_{4.85}$Sn$_{0.15}$ ball-milled for 1 hour.

Figure 42 shows the morphology of the particles of LiAlH$_4$ + LaNi$_{4.85}$Sn$_{0.15}$ taken in 1:1 volume ratio and ball-milled for 6 hours. The particle size distribution varies from less than 1 to 20 μm. It seems the smaller particles of the products formed during the decomposition of LiAlH$_4$ are attached to the surface of the larger particles of LaNi$_{4.85}$Sn$_{0.15}$. This may also explain the slow hydrogen absorption by this sample.
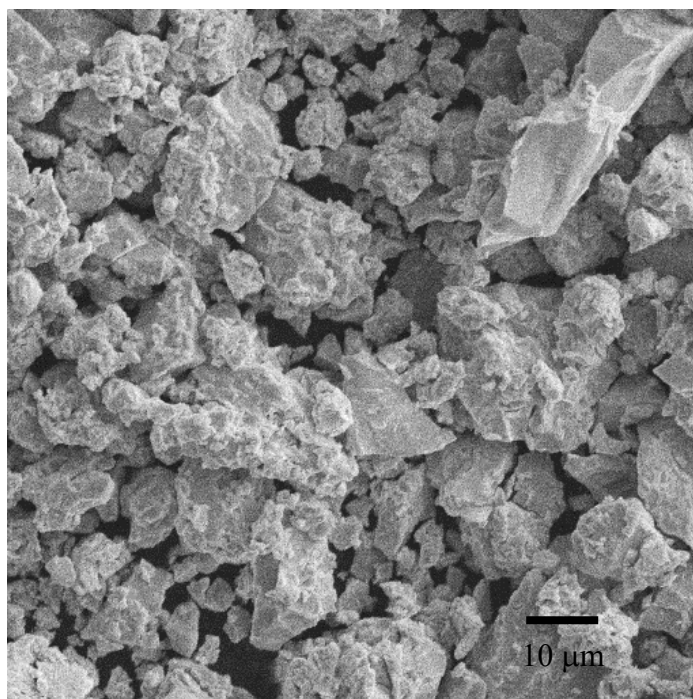
Figure 41. Morphology of pure LaNi$_{4.85}$Sn$_{0.15}$ ball-milled for 6 hours.

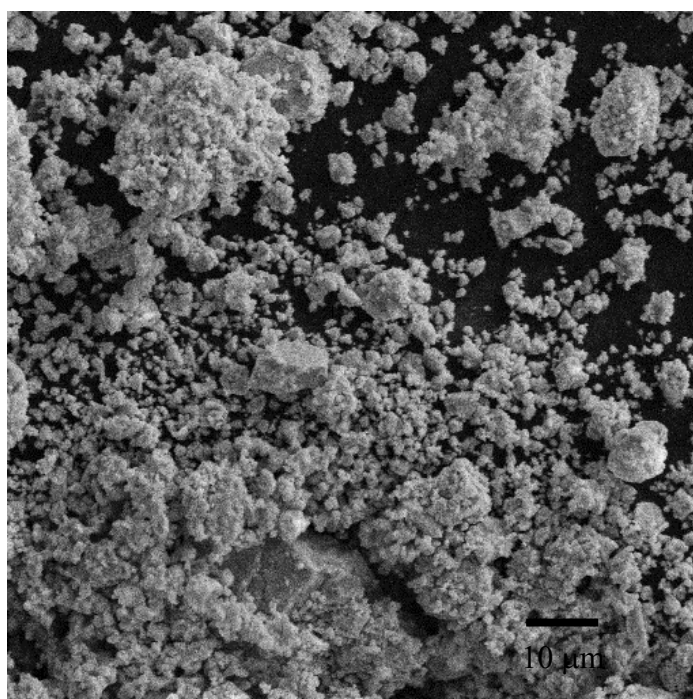Figure 42. Morphology of LiAlH$_4$ + LaNi$_{4.85}$Sn$_{0.15}$ taken in 1:1 volume ratio and ball-milled for 6 hours.

3.3 LiAlH$_4$ + Al$_3$Ti

Figure 43 shows the result of the XRD measurement of arc-melted Al$_3$Ti. The space group is I4/mmm and the lattice parameters are a=3.8563 (3) Å, c=8.6000 (8) Å.
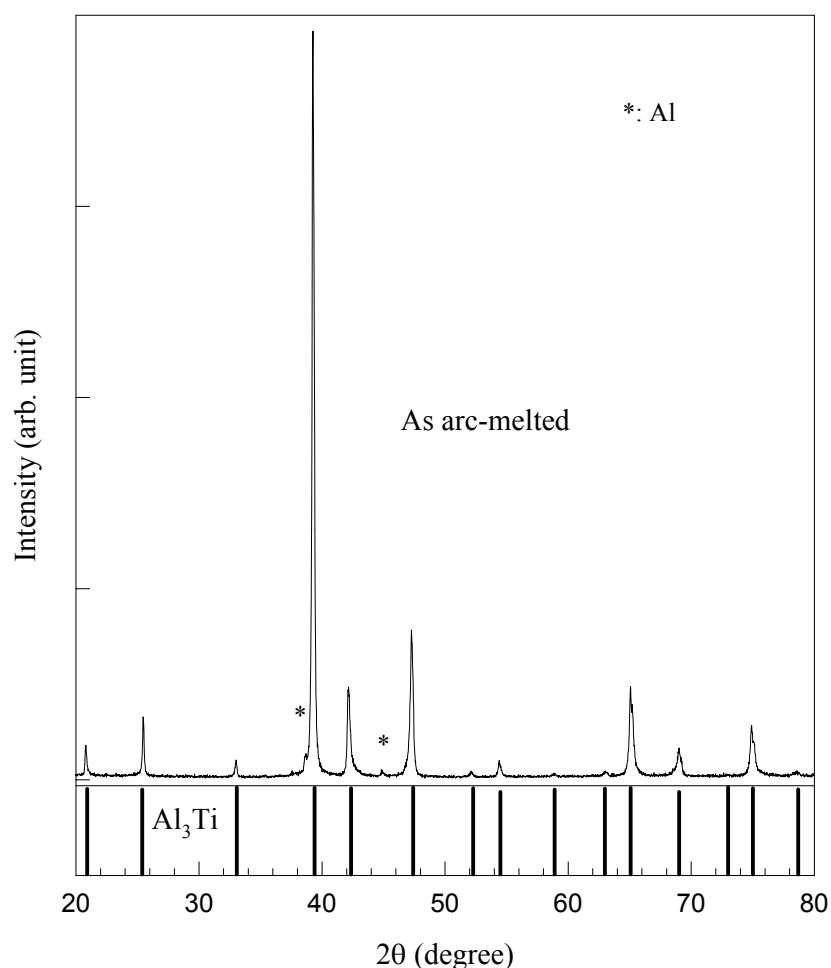

Figure 43. The XRD pattern of arc-melted Al$_3$Ti.

Figure 44 shows the results of the XRD measurements of pure LiAlH$_4$, LiAlH$_4$ + 3 mol% Al$_3$Ti ball-milled for 7 hours, and pure Li$_3$AlH$_6$. LiAlH$_4$ + 3 mol% Al$_3$Ti ball-milled for 7 hours mainly consists of LiAlH$_4$, Al$_3$Ti, Al and/or LiH. The Bragg peaks of Al and LiH overlap too much to be clearly distinguished. The peaks of Li$_3$AlH$_6$ are clearly visible, but they are weak.
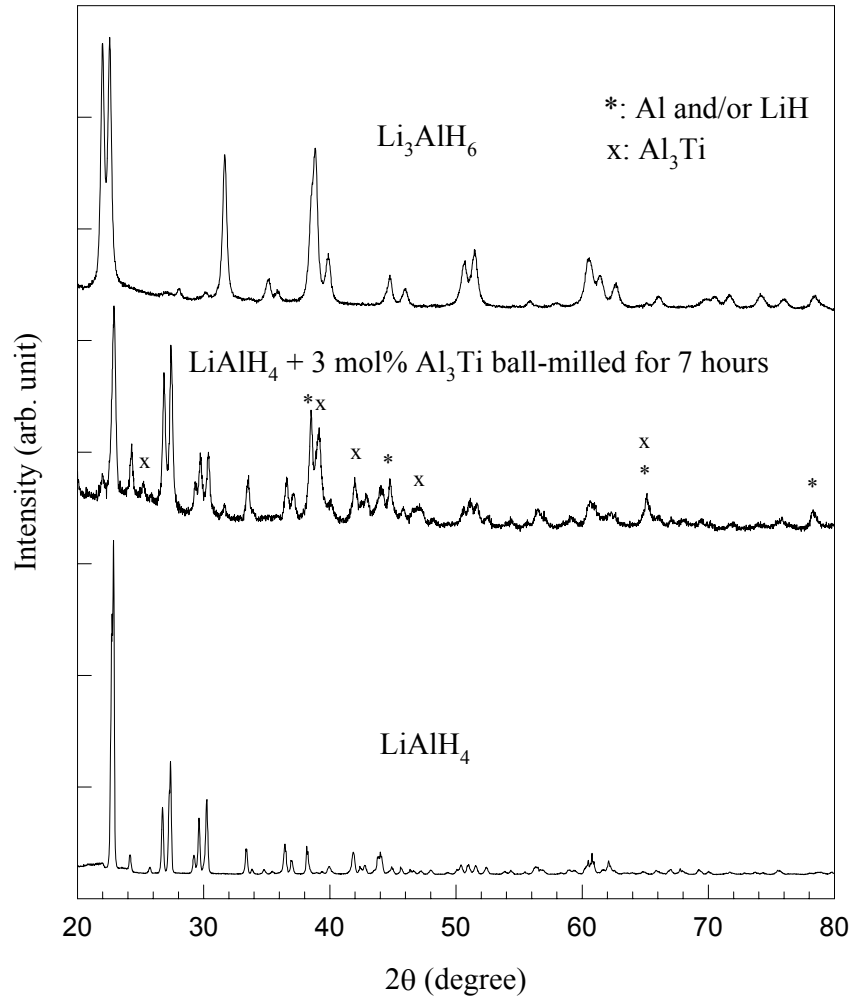
Figure 44. The XRD patterns of pure LiAlH₄ [21], LiAlH₄ + 3 mol% Al₃Ti ball-milled for 7 hours, and pure Li₃AlH₆ [21].

Figure 45 shows the results of the XRD measurements of LiAlH₄ + 3 mol% Al₃Ti ball-milled for 7 hours and then heated to 300 °C for 15 min, and ball-milled for 7 hours, heated to 300 °C for 15 min, and then hydrogenated at high pressure, 1000 psi ($\approx$ 68 atm.), at elevated temperatures, 50, 80, 100, and 130 °C, for 12, 13, 17, and 11 hours, respectively. Only the peaks for Al and/or LiH are found. Therefore, it seems that no hydrogenation occurs at these conditions.
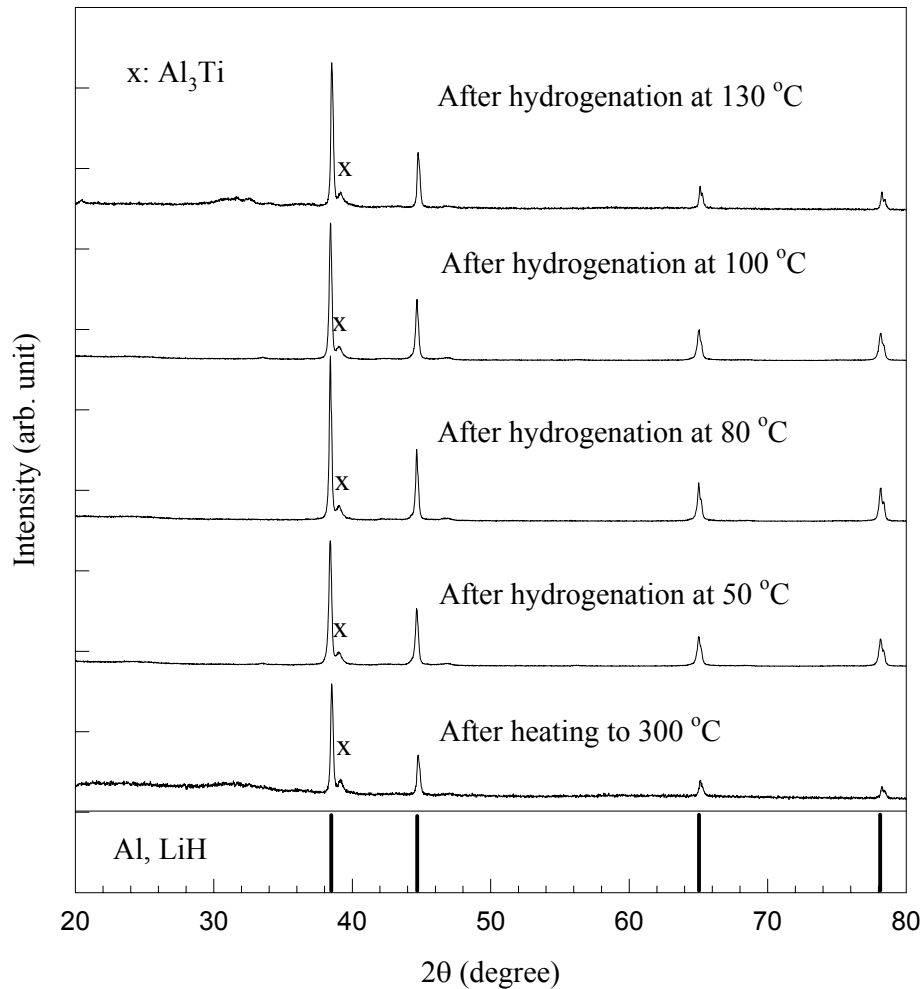
59

Figure 45. The XRD patterns of LiAlH$_4$ + 3 mol% Al$_3$Ti ball-milled for 7 hours and then heated to 300 ^{o}C for 15min, and ball-milled for 7 hours, heated to 300 ^{o}C, and then hydrogenated at 68 atm pressure at 50, 80, 100, and 130 ^{o}C.

Figure 46 shows the results of the DTA measurements of LiAlH$_4$ + 3 mol% Al$_3$Ti ball-milled for 7 hours, and ball-milled for 7 hours and then heated to 300 ^{o}C for 15 min. After ball-milling for 7 hours, the anomalies associated with the decomposition of LiAlH$_4$ (125 ^{o}C) and Li$_3$AlH$_6$ (210 ^{o}C) are found. However, the anomaly associated with the melting of LiAlH$_4$ is not found. This result is consistent with the work done by Balema et al. [24]. After heating to 300 ^{o}C no anomalies are found. This confirms that LiAlH$_4$ decomposes into LiH, Al, and H$_2$ completely after heating to 300 ^{o}C for 15 min.

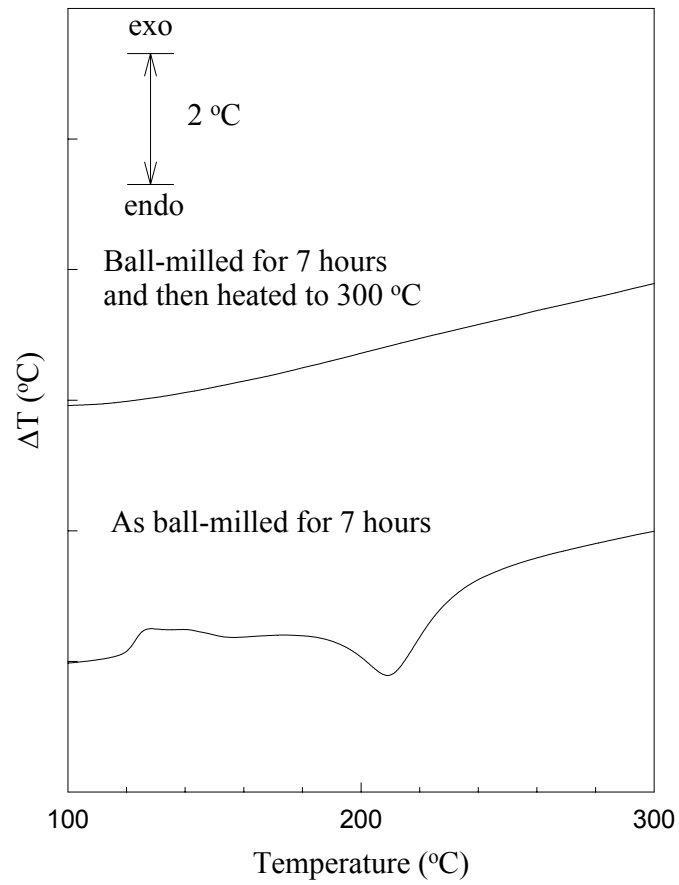Figure 46. The DTA traces of LiAlH$_4$ + 3 mol% Al$_3$Ti ball-milled for 7 hours and ball-milled for 7 hours and then heated to 300 ^{o}C for 15 min.

3.4 LiAlH$_4$ + PdCl$_2$

Figure 47 shows the results of the XRD measurements of pure LiAlH$_4$, LiAlH$_4$ + 3 mol% PdCl$_2$ ball-milled for 7 hours, and pure Li$_3$AlH$_6$. LiAlH$_4$ + 3 mol% PdCl$_2$ ball-milled for 7 hours mainly consists of LiAlH$_4$ and Al and/or LiH. The Bragg peaks corresponding to Li$_3$AlH$_6$ are considerably weaker than those of LiAlH$_4$ + 3 mol% Al$_3$Ti ball-milled for 7 hours. This indicates that Al$_3$Ti is a better catalyst of the mechanochemical decomposition of LiAlH$_4$ than PdCl$_2$. There are two Bragg peaks, which can not be identified with any known phase(s).
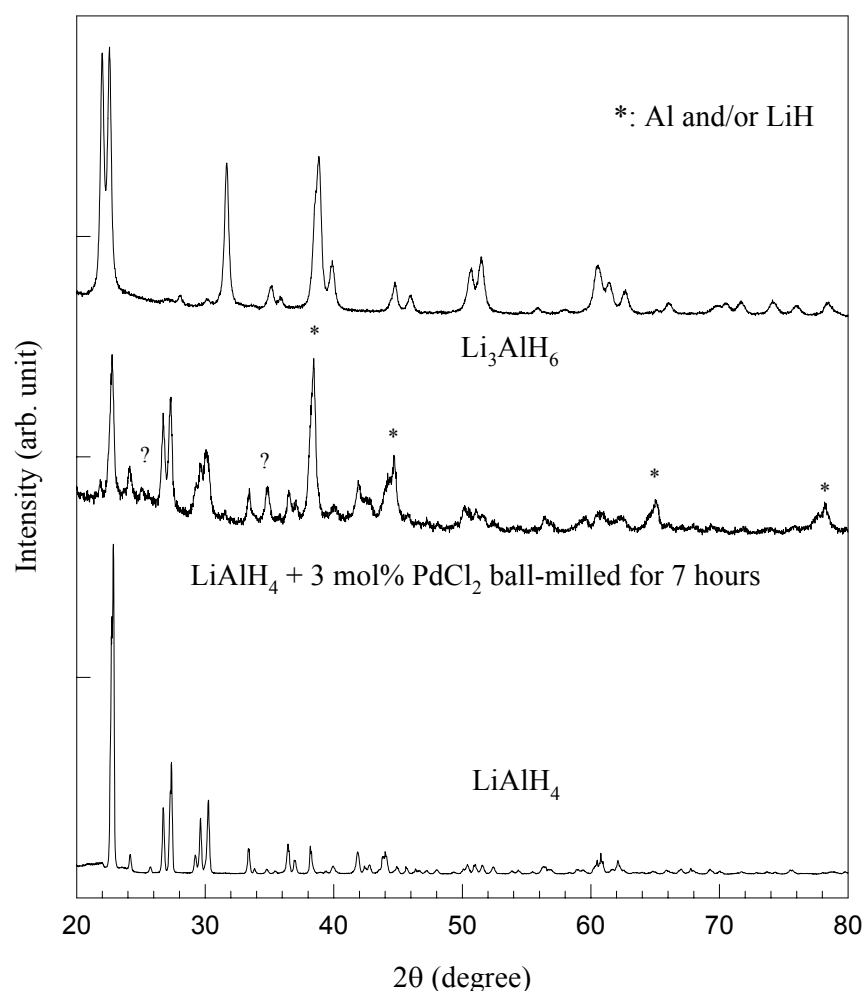

Figure 47. The XRD patterns of pure LiAlH$_4$ [21], LiAlH$_4$ + 3 mol% PdCl$_2$ ball-milled for 7 hours, and pure Li$_3$AlH$_6$ [21].

Figure 48 shows the result of the XRD measurements of LiAlH$_4$ + 3 mol% PdCl$_2$ ball-milled for 7 hours and heated to 300 ^{o}C and held at this temperature for 15 min, and ball-milled for 7 hours, heated to 300 ^{o}C, and then hydrogenated at high pressure, 1000 psi ($\approx$ 68 atm.), at elevated temperature, 80 and 100 ^{o}C, for 16 and 20 hours, respectively. The major peaks are identified with those of Al and/or LiH. Therefore, it appears that no hydrogenation occurs at these conditions. There are several minor Bragg peaks which can not be identified with any known phase(s).
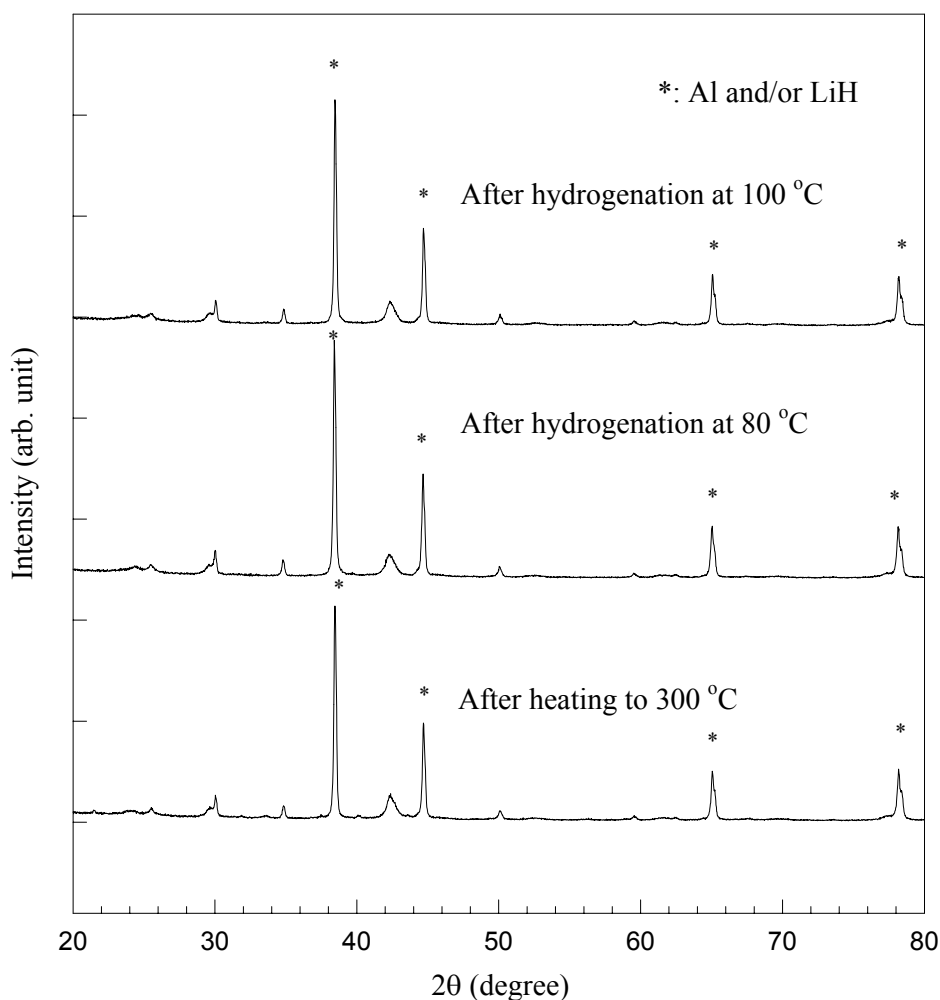

Figure 48. The XRD patterns of LiAlH$_4$ + 3 mol% PdCl$_2$ ball-milled for 7 hours and then heated to 300 ^{o}C for 15min, and ball-milled for 7 hours, heated to 300 ^{o}C, and then hydrogenated at 68 atm pressure at 80 and 100 ^{o}C.

Figure 49 shows the results of the DTA measurements of $LiAlH_4$ + 3 mol% $PdCl_2$ ball-milled for 7 hours, and ball-milled for 7 hours and then heated to 300 ^oC for 15 min. After ball-milling for 7 hours, the anomalies indicating the decomposition of $LiAlH_4$ and Li_3AlH_6 are found. Furthermore, there is an endothermic peak corresponding to melting of $LiAlH_4$ (140-170 ^oC). Hence, $PdCl_2$ is not a good catalyst, as discussed earlier. After heating to 300 ^oC, no anomalies are found, which indicates that $LiAlH_4$ decomposes into LiH, Al, and H_2 completely after heating to 300 ^oC for 15 min.
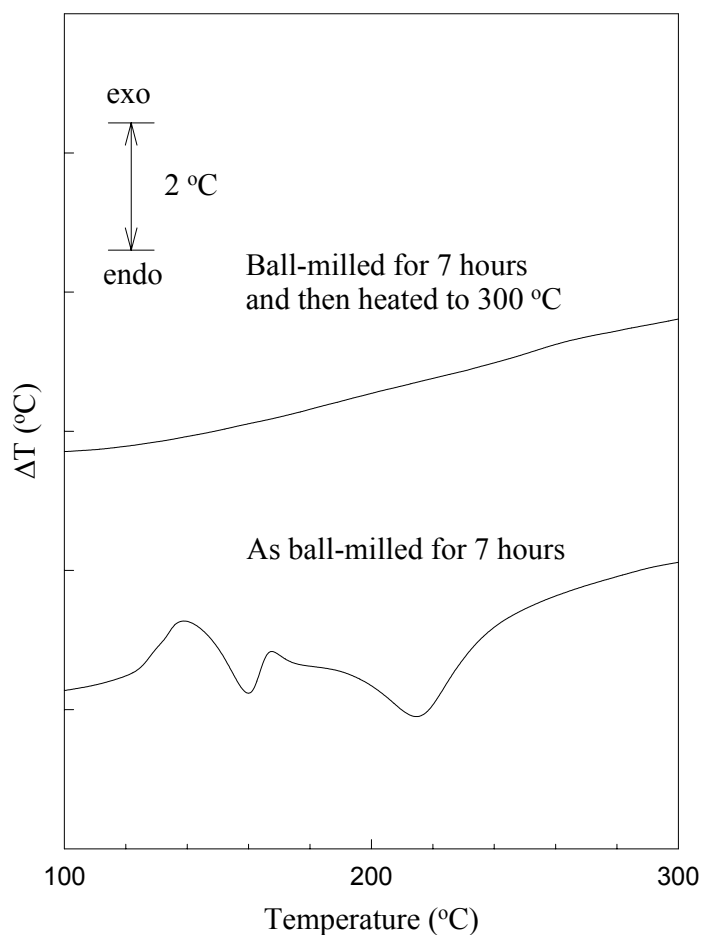

Figure 49. The DTA traces of $LiAlH_4$ + 3 mol% $PdCl_2$ ball-milled for 7 hours and ball-milled for 7 hours and then heated to 300 ^oC for 15 min.

4. CONCLUSIONS

$Zr_{27}Ti_9Ni_{38}V_5Mn_{16}Cr_5$, $LaNi_{4.85}Sn_{0.15}$, Al_3Ti, and $PdCl_2$ were examined as potential catalysts to enable $LiAlH_4$ to both absorb and desorb hydrogen near ambient conditions. Although all four materials worked as catalysts in the dehydrogenation reactions of both $LiAlH_4$ and Li_3AlH_6 by inducing the decomposition at lower temperature, none of them is applicable as catalysts in the reverse hydrogenation reaction at mild conditions (<70 atm H_2).

$LiAlH_4$ decomposes into Li_3AlH_6, Al, and H_2 at 160-190 ^{o}C without melting and Li_3AlH_6 decomposes into LiH, Al, and H_2 at 190-230 ^{o}C by mixing with the same volume of $Zr_{27}Ti_9Ni_{38}V_5Mn_{16}Cr_5$ and ball-milling for 1 hour. However, the products do not absorb hydrogen at low pressure after the decomposition. $Zr_{27}Ti_9Ni_{38}V_5Mn_{16}Cr_5$ does not absorb hydrogen either. This seems to be due to the lack of the activation.

$LiAlH_4$ decomposes into Li_3AlH_6, Al, LiH and H_2 during ball-milling for 6 hours with the same volume of $Zr_{27}Ti_9Ni_{38}V_5Mn_{16}Cr_5$. However, the products do not absorb hydrogen at low pressure after the decomposition. Instead, $Zr_{27}Ti_9Ni_{38}V_5Mn_{16}Cr_5$ absorbs about 0.9 wt% H_2. This seems to be due to the improvement of the surface of the sample particles.

$LiAlH_4$ decomposes into Li_3AlH_6, Al, and H_2 during ball-milling for 1 hour and into LiH, Al, and H_2 at 180-280 ^{o}C by mixing with the same volume of $LaNi_{4.85}Sn_{0.15}$. However, the products do not absorb hydrogen at low pressure after the decomposition. Instead, $LaNi_{4.85}Sn_{0.15}$ absorbs about 0.6 wt% H_2. This seems to be due to the presence of amorphous phases of $LaNi_{4.85}Sn_{0.15}$.

$LiAlH_4$ decomposes into Li_3AlH_6, Al, LiH, and H_2 during ball-milling for 6 hours with the same volume of $LaNi_{4.85}Sn_{0.15}$. However, the products do not absorb hydrogen at low pressure after the decomposition. $LaNi_{4.85}Sn_{0.15}$ does not absorb much hydrogen. This is because the LaH_2 phases become dominant after 6 hours mechanochemical processing and only a small portion of $LaNi_5$-based phase exists in the mixture.

LiAlH$_4$ was decomposed into Li$_3$AlH$_6$, Al, and H$_2$ at 130-150 ^{o}C without melting and Li$_3$AlH$_6$ was decomposed into LiH, Al, and H$_2$ at 180-240 ^{o}C by mixing with 3 mol% of Al$_3$Ti and ball-milling for 7 hours. Re-hydrogenation was attempted at high pressure, 1000 psi ($\approx$ 68 atm.) H$_2$, at elevated temperatures, 50, 80, 100, and 130 ^{o}C. However, the reverse hydrogenation reaction did not occur.

LiAlH$_4$ was decomposed into Li$_3$AlH$_6$, Al, and H$_2$ at 170-180 ^{o}C after its melting and Li$_3$AlH$_6$ was decomposed into LiH, Al, and H$_2$ at 180-240 ^{o}C by mixing with 3 mol% of PdCl$_2$ and ball-milling for 7 hours. Re-hydrogenation was attempted at high pressure, 1000 psi ($\approx$ 68 atm.) H$_2$, at elevated temperatures, 80 and 100 ^{o}C. As in the case of Al$_3$Ti, the reverse hydrogenation reaction did not occur.

REFERENCES

[1]   B. Bogdanovic, and M. Schwickardi, "Ti-doped alkali metal aluminium hydrides as potential novel reversible hydrogen storage materials," *J. Alloys and Compounds*, vol. 1, 1997, pp. 253-254.

[2]   B. Bogdanovic, R.A. Brand, A. Marjanovic, M. Schwickardi, and J. Toelle, "Metal-doped sodium aluminium hydrides as potential new hydrogen storage materials," *J. Alloys and Compounds*, vol. 302, 2000, pp. 36-58.

[3]   T. D. Durbin, "Hydrogen Engines and Vehicles: Characteristics and Development," *Hydrogen Fuel for Surface Transportation*, J. M. Norbeck, J. W. Heffel, T. D. Durbin, B. Tabbara, J. M. Bowden, and M. C. Montano, editors, Society of Automotive Engineers, Inc., Pennsylvania, 1996, pp. 5-25.

[4]   S. Furuhama, "Trend of Social Requirements and Technological Development of Hydrogen-Fueled Automobiles," *Hydrogen Fuel for Surface Transportation*, J. M. Norbeck, J. W. Heffel, T. D. Durbin, B. Tabbara, J. M. Bowden, and M. C. Montano, editors, Society of Automotive Engineers, Inc., Pennsylvania, 1996, pp. 37-46.

[5]   S. Thomas, and M. Zalbowitz, *Fuel cells. Green power*, Los Alamos, 1999.

[6]   A. J. Appleby, "Characteristics of Fuel Cell Systems," *Fuel Cell Systems*, L. J. M. J. Blomen, and M. N. Mugerwa, editors, Plenum Press, New York, 1993, pp. 157-199.

[7]   E. Barendrecht, "Electrochemistry of Fuel Cells," *Fuel Cell Systems*, L. J. M. J. Blomen, and M. N. Mugerwa, editors, Plenum Press, New York, 1993, pp. 73-119.

[8]   P. Pietrogrande, and M. Bezzeccheri, "Fuel Processing," *Fuel Cell Systems*, L. J. M. J. Blomen, and M. N. Mugerwa, editors, Plenum Press, New York, 1993, pp. 121-156.

[9]   S. S. Murthy, and M. Ramgopal, "Metal Hydride Refrigerators, Heat Pumps and Heat Transformers," *METAL HYDRIDES*, M. V. C. Sastri, B. Viswanathan, and S. S. Murthy, editors, Narosa Publishing House, New Delhi, 1998, pp. 106-145.

[10]   B. Scrosati, "Rechargeable lithium cells," *Modern Batteries – An Introduction to Electrochemical Power Sources Second Edition*, C. A. Vincent, and B. Scrosati, editors, John Wiley & Sons Inc., New York, 1997, pp. 198-242.

[11]   F. Bonino, and C. A. Vincent, "Secondary alkaline cells," *Modern Batteries – An Introduction to Electrochemical Power Sources Second Edition*, C. A. Vincent, and B. Scrosati, editors, John Wiley & Sons Inc., New York, 1997, pp. 162-197.

[12]   M. V. C. Sastri, "Chemical Applications of Metal Hydrides: Separation of Hydrogen From Gas Mixtures," *METAL HYDRIDES*, M. V. C. Sastri, B. Viswanathan, and S. S. Murthy, editors, Narosa Publishing House, New Delhi, 1998, pp. 152-157.

[13]   M. V. C. Sastri, "Introduction to Metal Hydrides: Basic Chemistry and Thermodynamics of Their Formation," *METAL HYDRIDES*, M. V. C. Sastri, B. Viswanathan, and S. S. Murthy, editors, Narosa Publishing House, New Delhi, 1998, pp. 1-21.

[14]   H. Buchner, "THE HYDROGEN/HYDRIDE ENERGY CONCEPT," *International J. Hydrogen Energy*, vol. 3, 1978, pp. 385-406.

[15]   L. Zaluski, A. Zaluska, and J.O. Stroem-Olsen, "Hydrogenation properties of complex alkali metal hydrides fabricated by mechano-chemical synthesis," *J. Alloys and Compounds*, vol. 290, 1999, pp. 71-78.

[16]   J. A. Dilts, and E. C. Ashby, "A Study of the Thermal Decomposition of Complex Metal Hydrides," *Inorganic Chemistry*, vol. 11, no. 6, 1972, pp. 1230-1236.

[17]   T. N. Dymova, D. P. Aleksandrov, V. N. Konoplev, T. A. Silina, and A. S. Sizareva, "Spontaneous and Thermal Decomposition of Lithium Tetrahydroaluminate $LiAlH_4$: The Promoting Effect of Mechanochemical Action on the Process," *Russian J. Coordination Chemistry*, vol. 20, no. 4, 1994, pp. 263-268.

[18]   T. N. Dymova, V. N. Konoplev, D. P. Aleksandrov, A. S. Sizareva, and T. A. Silina, "A

Novel View of the Nature of Chemical- and Phase-Composition Modifications in Lithium Hydridoaluminates $LiAlH_4$ and Li_3AlH_6 on Heating," *Russian J. Coordination Chemistry*, vol. 21, no. 3, 1995, pp. 165-172.

[19]   V. P. Balema, K. W. Dennis, and V. K. Pecharsky, "Rapid solid-state transformation of tetrahedral $[AlH_4]^-$ into octahedral $[AlH_6]^{3-}$ in lithium aluminohydride," *Chemical Communications*, 2000, pp. 1665-1666.

[20]   Z. Shi, "Microstructural characterization of a Zr-Ti-Ni-Mn-V-Cr based AB_2-type battery alloy," Iowa State University Master Thesis, 1999.

[21]   V. P. Balema (private communication).

[22]   K. Morii, and T. Shimizu, "Hydriding characteristics in $(Ti,Zr)(Ni,Mn,X)_2$ alloys," *J. Alloys and Compounds*, vol. 231, 1995, pp. 524-527.

[23]   M. V. C. Sastri, "Disproportionation Effects in $LaNi_5$ During Prolonged Cycling with Hydrogen," *METAL HYDRIDES*, M. V. C. Sastri, B. Viswanathan, and S. S. Murthy, editors, Narosa Publishing House, New Delhi, 1998, pp. 106-145.

[24]   V. P. Balema, J. W. Wiench, K. W. Dennis, M. Pruski, and V. K. Pecharsky, "Titanium catalyzed solid-state transformations in $LiAlH_4$ during high-energy ball-milling," *J. Alloys and Compounds*, vol. 329, 2001, pp. 108-114.

ACKNOWLEDGMENTS